THE ASTROPHYSICAL JOURNAL, 403:810–832, 1993 February 1

AVERAGE EFFECTS OF LARGE-SCALE CONVECTION ON HELIOSEISMIC LINE WIDTHS AND FREQUENCIES

EUGENE M. LAVELY
High Altitude Observatory and Advanced Study Program, National Center for Atmospheric Research, P.O. Box 3000, Boulder, CO 80307-3000
AND
MICHAEL H. RITZWOLLER
Department of Physics, University of Colorado, Campus Box 390, Boulder, CO 80309-0390
Received 1992 April 6; accepted 1992 July 31

ABSTRACT

We present the numerical application of the theoretical formalism of Lavely & Ritzwoller (1992) to the model of stationary, large-scale solar convection described by Glatzmaier (1984) in order to search for a useful characteristic signature of giant-cell convection in helioseismic data. The numerical results contain two major simplifications. First, they are based on degenerate perturbation theory rather than the more accurate quasi-degenerate perturbation theory, with the consequence that only the toroidal component of flow has a helioseismic effect. Second, to insulate these synthetic experiments from explicitly simulating the source of helioseismic oscillations, we present ensemble average results, the average effect of convection on helioseismic data taken over a large number of observing intervals. Frequency and line-width measurements are presented on spatially filtered spectra, so that references to azimuthal orders apply to the m-value of the spherical harmonic, Y_l^m, of the spatial filter. Frequency splittings are antisymmetric in m and are maximum for large $|m|/l$. They are not well fitted by a low-degree Legendre polynomial and are below the currently measurable level for Glatzmaier's model of convection. Systematic patterns exist in radial order and harmonic degree which may be able to be exploited observationally. The most significant helioseismic signature of Glatzmaier's model of large-scale convection is a systematic apparent line-broadening effect which is dominantly parabolic in m (the azimuthal order of the spherical harmonic spatial filter) within each multiplet, so that line widths are maximum for low-$|m|/l$ states and are relatively unaffected for high-$|m|/l$ states. We call this pattern the Q-bowl. The size of this line-broadening effect scales with average convective velocity and degenerate Q. Since Glatzmaier's model is defined only to 0.95 $R_\odot$ and since we ignore poloidal flows, the helioseismic effects of Glatzmaier's model may be considered conservative. To offset this fact, we have set intrinsic Q to be high (10^4), consistent with very low frequency degenerate Q measurements, and to be constant with frequency, although Q-values above 2 mHz are considerably lower than this. Line broadening for certain nearly zonal ($m = 0$) resonances exceeds 50% of this input intrinsic Q for Glatzmaier's model. In addition, the measured apparent degenerate Q of each multiplet is systematically reduced by convection. The magnitude of these effects is dependent on the intrinsic Q, on harmonic degree l, and on the degenerate frequency of the multiplet. Increasing the size of the nonaxisymmetric part of the flow model acts to depress degenerate Q further and broadens the Q-bowl. To establish the existence of convective giant cells, and, perhaps, to estimate their statistical characteristics, it should become an observational priority to measure individual m-state line widths or line-width trends within multiplets. Current Q measurements have been made by linearly recombining the $(2l + 1)$ resonances within a multiplet to produce a high signal-to-noise measurement of degenerate Q. Our predictions on the systematics of measurements of degenerate Q in the presence of large-scale convection are consistent with these observations.

Subject headings: convection — line: profiles — Sun: oscillations

1. INTRODUCTION

The promise for the use of helioseismic data to reveal new information about the solar interior remains strong. Nowhere is this more true than in the potential for the use of helioseismic data to constrain the properties of large-scale convection deep in the solar interior. Nevertheless, with the exception of estimates of the axisymmetric component of large-scale convection, differential rotation (e.g., Brown et al. 1989; Christensen-Dalsgaard, Schou, & Thompson 1990; Thompson 1990; Ritzwoller & Lavely 1991), comparatively little emphasis has been placed on this problem to date (e.g., Hill, Toomre, & November 1983; Brown 1984; Hill 1988, 1989; Bogdan 1989; Balmforth 1992a, b, c; Lavely & Ritzwoller 1992).

In this paper we do not propose to solve the helioseismic inverse problem for convection. Instead, we continue to investigate the forward problem on which the inverse problem must surely rest and study the helioseismic effects of a single model of convection in detail. We present numerical estimates of the influence of a global-scale, steady state convective flow field on helioseismic data—in particular, on modal frequencies and line widths. It is intended that this work should provide part of the necessary background for future attacks on the inverse problem by determining the signature(s) of convection in helioseismic data. If the characteristic signature(s) of convection should be observed, they would provide evidence for the existence of large-scale convection in the deep interior of the convection zone. In addition, estimation of these signatures could be used as data in future inversions to constrain deep-seated

solar convection. Helioseismic constraints on the large-scale dynamics of the solar interior would constrain convection theories and, for example, should help dynamicists assess the relation between solar convection and both the solar dynamo and the observed large-scale solar magnetic activity.

Thus, the goal of this study is to aid in the understanding of solar convection by using helioseismic data to constrain convection deep in the solar interior. This paper is preceded by a purely theoretical treatment of the forward problem by Lavely & Ritzwoller (1992). The results of the current paper differ from those of our subsequent studies in two principal ways. We concentrate here on the average effects of convection on helioseismic data, and we ignore observational artifacts such as cross talk, day/night sidelobes, noise, and so on. Given an ensemble of helioseismic observation intervals and a stationary convective field, by *average* we mean the expected value of the effect of convection on helioseismic data taken over all, or at least a great many, time intervals. We will refer to a single observing interval as a *single realization.* The helioseismic effects discussed here are called *ensemble-average effects*, and we speak of frequency and line-width measurements made in the *ensemble average.* As will be expanded upon below, single observing intervals will not produce ensemble-average estimates of helioseismic observables. Kelly & Ritzwoller (1993) discuss how spectral estimates from single realizations can be made to approximate the ensemble average and also discuss the effects of observational artifacts ignored here.

We consider ensemble-average effects here for two reasons. First, the ensemble-average effects are more simply related to the input convective model. Thus, it is these effects that we wish first to understand and later to estimate to constrain convection. Second, as we will show below, doing so frees us from explicitly simulating the source of helioseismic oscillations.

1.1. *Models of Solar Convection*

The convective velocity field used in our computations was computed by G. Glatzmaier in a numerical simulation of large-scale solar convection and is described here in § 2.1. The reader is referred to Glatzmaier (1984) for a description of the equations governing solar convection and the numerical methods he used to solve them. A recent review of solar convection can be found in Spruit, Nordlund, & Title (1990). Although our numerical results are for a specific numerical model of convection, the methodology that we have introduced to calculate helioseismic time series, power spectra, line widths, and frequencies in a convecting model can be applied to any numerical model of convection whose scalar and vector variables can be parameterized in terms of scalar or vector global spherical harmonics, and whose properties satisfy the theoretical assumptions on the splitting matrix listed in § 3. In addition, although the magnitude and details of the effects of different convection models will vary, the general character of the effects that we stress here will be the same. As described in § 2.1, Glatzmaier's convective model is ideally suited as a basis model for our simulations. However, it is only defined from slightly below the base of the convection zone (since it models convective overshoot) outward to approximately 0.95 $R_\odot$, where $R_\odot$ is the solar radius. Since this model does not contain the strong near-surface flows, its predictions of convective effects on helioseismic data should be considered conservative. To mitigate this fact, we have chosen input intrinsic Q to be higher than measured intrinsic Q above 2 mHz. With an intrinsic Q of 10^4 we show that Glatzmaier's model produces a strong, systematic signal in helioseismic line widths (which, using the method of Kelly & Ritzwoller 1993, may be observable at low frequencies) but a weaker one in frequencies which are below the level of current measurements.

In Lavely & Ritzwoller (1992) we discussed observational evidence that is suggestive of the existence of coherent, large-scale flows in the deep interior of the convection zone. However, recent numerical simulations of convection by Stein & Nordlund (1989) and Cattaneo et al. (1991) demonstrate that coherent structures near the top of the turbulent boundary-layer model disintegrate into increasing disorganized motions with depth. These simulations only model flows near the solar surface and are outside of the depth regime that we consider here and that is modeled by Glatzmaier. The question of the existence of sustained, organized flow structures at depth remains an open area of research and will ultimately be answered only observationally. This is the prime motivation for the present study.

1.2. *Modeling the Effect of Convection on Helioseismic Data*

The effect of convection on helioseismic data can be modeled in a variety of ways. From a ray-theoretic point of view, convection perturbs propagation speeds and alters ray trajectories. Hill et al. (1983) and Hill (1988, 1989) have developed and applied ray-theoretic concepts to model the influence of near-surface convection on waves confined to the upper part of the convection zone. From a modal-theoretic point of view, convection couples modes from the reference state, the spherically symmetric, nonrotating, nonmagnetic, adiabatic, isotropic, static (SNRNMAIS) solar model, and splits frequencies. In terms of traveling waves, coupling corresponds to deflection and deformation of wave fronts. Splitting corresponds to path-dependent speeding up and slowing down of waves. We follow Lavely & Ritzwoller (1992), who presented a general modal theory using quasi-degenerate perturbation theory to model the influence of global-scale convection on modal coupling and splitting. In this theory, modes of the SNRNMAIS solar model that are nearly degenerate in frequency are allowed to couple. For numerical simplicity, here we use degenerate perturbation theory, described in § 3 and Appendix B, which is a special case of the quasi-degenerate perturbation theory. Under degenerate perturbation theory, only those modes with the same degenerate frequency in the SNRNMAIS model can couple. That this restricts the number of possible coupling partners provides another reason why the results presented here should be considered conservative. In particular, as discussed in § 7 of Lavely & Ritzwoller (1992), under quasi-degenerate perturbation theory both poloidal and toroidal flows produce modal coupling and, therefore, potentially observable effects, whereas under degenerate perturbation theory only odd-degree toroidal flows couple modes.

The basis for our numerical simulations is the theoretical expression for the acoustic wave field, $\boldsymbol{u}_k(\boldsymbol{r}, t)$, for multiplet $k = (n, l)$, presented by Lavely & Ritzwoller (1992). The displacement field of multiplet k in the corotating frame generated by the σth source is given by

$$\boldsymbol{u}_k^\sigma(\boldsymbol{r}, t) = (\boldsymbol{s}_k^T \mathbf{A}^{(k)}) \exp\{i[\boldsymbol{\Lambda}^{(k)} + (\omega_k + i\alpha_k)\mathbf{I}]t\} * [\mathbf{A}^{(k)\dagger} \boldsymbol{a}^{\sigma,k}(t)], \quad (1)$$

where T and $\dagger$ denote, respectively, the transpose and adjoint operators, $\mathbf{I}$ is the identity matrix, $*$ denotes the convolution operator, $\boldsymbol{a}^{\sigma,k}(t)$ is the source vector defined below by equation

(3), ω_k is the degenerate frequency, $\alpha_k = \omega_k/(2Q_k)$ is the intrinsic attenuation rate, and Q_k is the intrinsic quality factor, s_k is the vector of displacement eigenfunctions s_k^m for $(-l \le m \le l)$, $\mathbf{A}^{(k)}$ is the eigenvector matrix that diagonalizes the splitting matrix $\mathbf{H}_k$, $\mathbf{\Lambda}^{(k)}$ is the diagonal matrix containing the eigenvalues of $\mathbf{H}_k$ and is defined in terms of $\mathbf{H}_k$ and $\mathbf{A}^{(k)}$ by equation (13). The total wave field for multiplet k is given by

$$\boldsymbol{u}_k(\boldsymbol{r}, t) = \sum_{\sigma} \boldsymbol{u}_k^{\sigma}(\boldsymbol{r}, t) , \tag{2}$$

where the sum is taken over all sources σ. Modal notation and terminology are discussed further in Appendix A.

The displacement eigenvector $\boldsymbol{s}_k$ and degenerate frequency ω_k in the linear theory are dependent solely on the reference SNRMAIS solar model and were computed using the method of Woodhouse (1988). The reference solar model was computed using a stellar evolution program written by R. Gilliland. Theoretical estimates of the quality factor Q_k are dependent on mechanisms that produce damping and auxiliary quantities such as turbulent viscosities, radiative opacities, the choice of the atmospheric model above the photosphere, the nature of convection-oscillation interaction, the inclusion of nonlinear effects, and so forth. Because of the increase in the effect of damping processes with frequency as modes compress near the surface, Q-values in the Sun decrease with frequency. Nevertheless, in most of our numerical experiments we will assume that Q is constant with frequency. We do this for two reasons. The first reason is simplicity, so that frequency-dependent Q effects caused by convection can be easily identified. Second, theoretical models of intrinsic Q (Christensen-Dalsgaard, Gough, & Libbrecht 1989) are at variance with observations and each other, and, as we will argue below, observed Q trends will be affected by apparent line broadening caused by convection. Therefore, choice of the nature of frequency dependence is not entirely straightforward. A more significant assumption than the constancy of intrinsic Q is our choice of its value, 10^4, which is about 5 times too large for modes between 2 and 3 mHz, but is consistent with very low frequency Q measurements (Libbrecht 1988). We have chosen a high Q-value in an attempt to offset the fact that we consider Glatzmaier's model of large-scale convection to be conservative. As will be shown below, convective line-broadening scales directly with convective velocity and Q.

Inspection of equation (1) reveals four principal challenges in simulating acoustic wave fields: (1) constructing the splitting matrix $\mathbf{H} = \mathbf{A}\mathbf{\Lambda}\mathbf{A}^{\dagger}$ (which is a function of the flow field), (2) simulating the source vector $\boldsymbol{a}^{\sigma,k}(t)$, (3) projecting onto a single spherical harmonic component of the displacement eigenfunction s_k^T by spatial filtering, and (4) making the spectral estimates of modal amplitudes, frequencies, and line widths. The flow field is discussed in § 2, and the construction and nature of the splitting matrix $\mathbf{H}$ is discussed in § 3. Calculation of power spectra and spectral estimation of modal amplitudes, frequencies, and line widths are discussed in § 4. The majority of the numerical results appear in § 5. In the remainder of § 1 we will primarily discuss the source vector and the spatial filter.

1.3. *The Acoustic Source Process*

We adopt here the currently prevailing view that solar acoustic modes are excited by acoustic noise generated by turbulent convection near the solar surface (Goldreich & Kumar 1988; Kumar & Goldreich 1989; Brown 1990; Balmforth 1992c). Goldreich & Kumar (1988) showed that acoustic emissions vary as the eighth power of the Mach number. Consequently, Brown (1990) suggested that most of the emission originates from that small fraction of the flow volume containing the very highest velocity flows. Observational support of Brown's model can be found in Goode, Gough, & Kosovichev (1992). Simple scaling arguments suggest that the characteristic spatial dimension of a source region is considerably smaller than the horizontal wavelengths of low- and intermediate-degree modes, and that the lifetime of a given source is comparable to typical modal periods. Therefore, Lavely & Ritzwoller (1992), in § 9, using the source representation theory of Backus & Mulcahy (1976a, b), assumed that the sources of acoustic energy are well approximated with delta functions in space, but retained the general time dependence of each source. The acoustic wave field is given by the convolution of the source time functions with the harmonic resonances of the convecting solar model. The dependence of the acoustic displacement field on the source process is modeled with the source vector $\boldsymbol{a}^{\sigma,k}(t)$ which describes the source time history of the σth source. The azimuthal order-m component of $\boldsymbol{a}^{\sigma,k}(t)$ is defined by the relation

$$a_m^{\sigma,k}(t) = \frac{-\boldsymbol{M}^{\sigma}(\boldsymbol{r}_{\sigma}, t) : \boldsymbol{e}^{(k,m)*}(\boldsymbol{r}_{\sigma})}{N_k \omega_k^2} , \tag{3}$$

where $\boldsymbol{M}^{\sigma}(\boldsymbol{r}_{\sigma}, t)$ is the moment rate tensor evaluated at the source centroid location $\boldsymbol{r}_{\sigma}$ of the σth source which is sufficient to represent a general dipolar and/or quadrupolar acoustic source, $\boldsymbol{e}^{(k,m)}$ is the strain tensor of the SNRNMAIS mode (n, l, m), and N_k is the normalization constant defined by equation (A4).

Three principal assumptions simplify the use of equations (1) and (3) presented here. First, the turbulent nature of the source process suggests that the components $a_m^{\sigma,k}$ of the source vectors at each time are uncorrelated. This is called the *random phase approximation* and was used, for example, by Kumar & Goldreich (1989) in their study of nonlinear modal interactions among solar p and f modes. Second, the observed equipartition of energy (Libbrecht, Woodard, & Kaufman 1990) among the $(2l + 1)$ m-states of a given multiplet implies that, on average, the modulus of the spectral density of $a_m^{\sigma,k}(t)$ is independent of m. Third, as discussed above, we seek here only ensemble-average spectral characteristics. As we will argue below, in the ensemble average the *source spectrum* (i.e., the power spectrum of the source time history) is constant over narrow frequency bands, i.e., it is locally approximately flat. Thus, seeking only ensemble-average effects allows us to ignore the time dependence of the source vectors. In a later contribution, we simulate the source time history and demonstrate that spectral estimates made on a large number of realizations do, indeed, converge to the ensemble average.

1.4. *Data Reduction and Helioseismic Observables*

The remaining undiscussed challenge is that we attempt to provide estimates of the effect of large-scale convection on aspects of helioseismic data similar to the form in which they are observed. Typically, observers spatially filter time sequences of helioseismic images, projecting each image onto a set of spherical harmonics to produce for each spherical harmonic degree and azimuthal order, Y_l^m, a single time series. This procedure is discussed further in § C2 below. We note that the result of the spatial filtering process can be approximated

by simply considering the time series for each spherical harmonic component of the displacement eigenfunction s_k^m in equation (1). Our procedure essentially produces a perfect spatial filter. It possesses no modal cross talk due to uneven sampling, no seeing effects, and no noise of any kind. We say that each such time series created by spatial filtering is associated with an *m-state*, or that the displacement pattern described by the spherical harmonic Y_l^m is an *m-state*. An understanding of what is meant by m here is crucial. In a spherical or axisymmetric model each m-state is associated with a single frequency, and, thus, an m-state is a single mode of oscillation. Inspection of equation (1) shows that each m-state in a convecting model is multiply periodic, being composed of $(2l + 1)$ individual harmonic functions. We call the cluster of $(2l + 1)$ unresolved Lorentzians (the power spectrum of a decaying, complex exponential in the time domain) *a generalized resonance function*. Typically, observers fit a single Lorentzian to each resonance function in the frequency domain. Since each generalized spectral "line" is actually composed of $(2l + 1)$ individual lines, the single Lorentzian model is imperfect. Therefore, we refer to the frequency and quality factor estimates of the Lorentzian fit to the generalized resonance function as the *apparent frequency*, ω_{app}, and the *apparent* Q, Q_{app}, of the generalized resonance function. The values taken by the apparent frequency and apparent Q estimates are dependent upon the method of fitting, since the fit is imperfect. This is discussed further in § 4.

Thus, the line-broadening effect of convection that is the focus of this paper is caused by the multiply periodic nature of each m-state. In a nonlinear theory, convection and acoustic oscillations can couple and convection can damp the oscillations and change the intrinsic Q of an acoustic mode. But our theory is linear, and convection and oscillations do not explicitly exchange energy. The line broadening we discuss in this paper is merely an apparent line broadening which results from the fact that the spectra being considered are for a single (l, m) pair, and there are multiple lines caused by coupling in each generalized resonance function. In our theory, the intrinsic Q of each individual mode of oscillation of the convecting model has not been changed by convection. However, we measure Q-values not on individual modal lines but on generalized resonance functions. It is these spatially filtered spectra which display the line-broadening effect.

1.5. *Overview of the Paper*

The paper is organized as follows. In § 2 we describe the convection and differential rotation models used in our numerical calculations. In § 3 we describe the numerical construction of the splitting matrix. In § 4 we derive an expression for the power spectrum of a generalized resonance function in the emsemble average and discuss the methods that we use to estimate apparent frequencies and line widths. In § 5 we present numerical estimates of these quantities, and we discuss the comparison between our predictions and existing observations in § 6. Technical discussions supportive of the arguments in the body of the text are included in the Appendices.

2. MODELS OF CONVECTION

Examples of numerical, global-scale models of convection include the models computed by Gilman & Glatzmaier (1981), Glatzmaier & Gilman (1981, 1982), Glatzmaier (1984), and Gilman & Miller (1986). These models share a number of characteristics that make them natural for use with the theory presented by Lavely & Ritzwoller (1992). First, the long-wavelength, deep-seated components of the flow fields in these numerical simulations are approximately stationary for substantial periods of time. Second, the models were computed in the anelastic approximation, and their maximum convective velocities are small enough to justify the assumption of linearity in our perturbation theory. Finally, the models are global in extent, and the convective variables of the models are parameterized in scalar and vector spherical harmonics which are used in our theory. The numerical model used in our calculations was computed by Glatzmaier (1984). In §§ 2.1 and 2.2 we describe, respectively, the nonaxisymmetric and axisymmetric components of the velocity field. In this paper, the *convecting model* is defined to include both nonaxisymmetric and axisymmetric velocity fields, whereas the *differentially rotating model* refers to the axisymmetric part of the convective velocity field alone.

2.1. *The Convective Velocity Field*

We represent the global-scale convective velocity field with vector spherical harmonics which are the natural basis functions for a vector field on or in a sphere. A general stationary, laminar velocity field $\boldsymbol{u}_0(r, \theta, \phi)$ can be decomposed into poloidal and toroidal components:

$$\boldsymbol{u}_0(r, \theta, \phi) = \sum_{s=0}^{\infty} \sum_{t=-s}^{s} [u_s^t(r) Y_s^t(\theta, \phi)\hat{\boldsymbol{r}} + v_s^t(r)\nabla_1 Y_s^t(\theta, \phi) - w_s^t(r)\hat{\boldsymbol{r}} \times \nabla_1 Y_s^t(\theta, \phi)] , \quad (4)$$

where the expansion coefficients $u_s^t(r)$ and $v_s^t(r)$ define the poloidal flow, and the coefficients $w_s^t(r)$ define the toroidal flow. The anelastic condition $\nabla \cdot [\rho_0 \boldsymbol{u}_0(r)] = 0$ constrains the poloidal expansion coefficients by the relation $\partial_r(r^2 \rho_0 u_s^t) = \rho_0 rs(s + 1)v_s^t$. The reality of the flow field and the relation $Y_s^{t*} = (-1)^t Y_s^{-t}$ imply that the radial expansion coefficients satisfy the conditions $u_s^{-t} = (-1)^t u_s^{t*}$, $v_s^{-1} = (-1)^t v_s^{t*}$, and $w_s^{-t} = (-1)^t w_s^{t*}$ where the asterisk here denotes complex conjugation.

Glatzmaier (1984) represents the convective velocity field in a form that conserves mass flux so that the velocity field automatically satisfies the anelastic condition. From equation (4a) of his paper, his representation of the flow field can be rewritten

$$\boldsymbol{v}(r, \theta, \phi) = \frac{1}{\rho_0(r)} \sum_{s=0}^{N} \sum_{t=-s}^{s} \nabla \times \nabla \times [\tilde{w}_s^t(r) Y_s^t(\theta, \phi)\hat{\boldsymbol{r}}] + \nabla \times [\tilde{z}_s^t(r) Y_s^t(\theta, \phi)\hat{\boldsymbol{r}}] . \quad (5)$$

Equating the r, θ, and ϕ components of $\boldsymbol{v}$ and $\boldsymbol{u}_0$, and using the orthogonality of the spherical harmonics, we obtain the following equalities:

$$u_s^t(r) = \frac{1}{r^2 \rho_0} s(s + 1)\tilde{w}_s^t(r) , \quad (6)$$

$$w_s^t(r) = \frac{1}{r\rho_0} \tilde{z}_s^t(r) , \quad (7)$$

$$v_s^t(r) = \frac{1}{r\rho_0} \frac{\partial \tilde{w}_s^t(r)}{\partial r} . \quad (8)$$

Equations (6) and (8) together yield a relation identical to the anelastic condition cited above.

We obtained the expansion coefficients $\tilde{w}_s^t(r)$, $\partial_r \tilde{w}_s^t(r)$, and $\tilde{z}_s^t(r)$ from Glatzmaier and transformed them using equations (6)–(8). Figure 1 displays the moduli of the expansion coeffi-

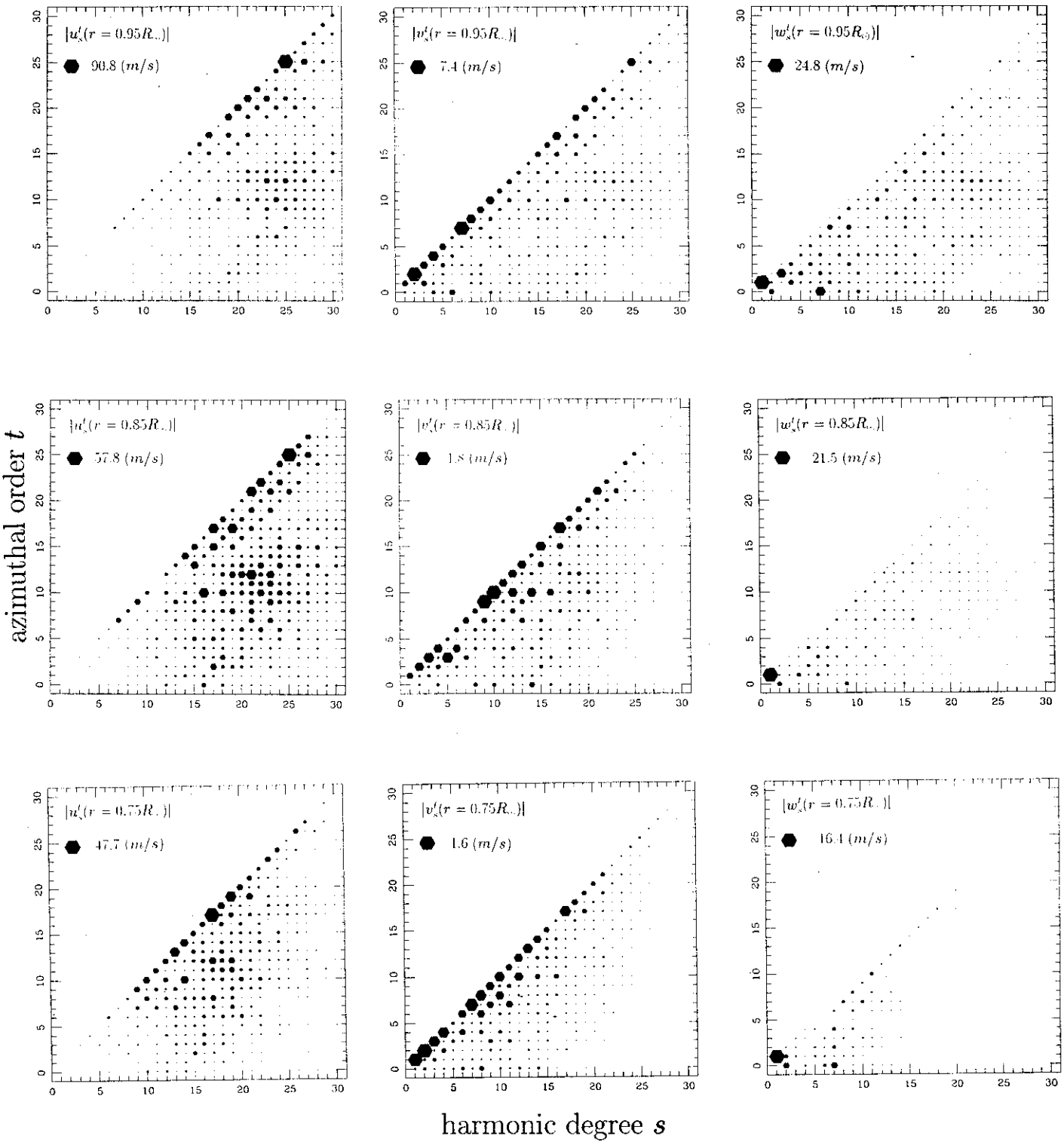

FIG. 1.—Modulus of the complex expansion coefficients $u_s^t(r)$, $v_s^t(r)$, and w_s^t (in meters per second) of Glatzmaier's model described in § 2.1, plotted at three different radial levels. *Top panels*: $r = 0.95\ R_\odot$, *middle panels*: $r = 0.85\ R_\odot$, *bottom panels*: $r = 0.75\ R_\odot$, corresponding respectively to the top, middle, and bottom of the convection zone. The size of each symbol is proportional to the size of the associated velocity coefficient, where size is normalized separately for each graph. As radius decreases, the velocity reduces and wavelengths increase. Most of the power in the poloidal coefficients, u_s^t and v_s^t, is concentrated in the sectoral components which can be identified with banana-cell type convection. For the toroidal field, w_s^t, the zonal ($t = 0$) expansion coefficients for $s = 1, 3, 5$ (which correspond to differential rotation) have been omitted, since their large size would overwhelm the features of this figure. Most of the power in the toroidal velocity field is in the longest wavelength components.

cients $u_s^t(r)$, $v_s^t(r)$, and $w_s^t(r)$ at the three radial levels, $r = 0.95\ R_\odot$, $r = 0.85\ R_\odot$, and $r = 0.75\ R_\odot$, for harmonic degrees $1 \le s \le 30$ and azimuthal orders $0 \le t \le s$. The sizes of the hexagons in each of these figures are proportional to the modulus of the coefficients. These coefficients represent the configuration of the velocity field at a single time step in Glatzmaier's numerical simulation. Glatzmaier evolved his convection model until initial transients died out and major components of the flow had reached approximately steady state conditions. The simulation contains spectral components extending to $s = 42$. We have truncated the plots in Figure 1 at $s = 30$, since the power in the components in the range $31 \le s \le 42$ is greatly diminished relative to the power in the longer wavelength components.

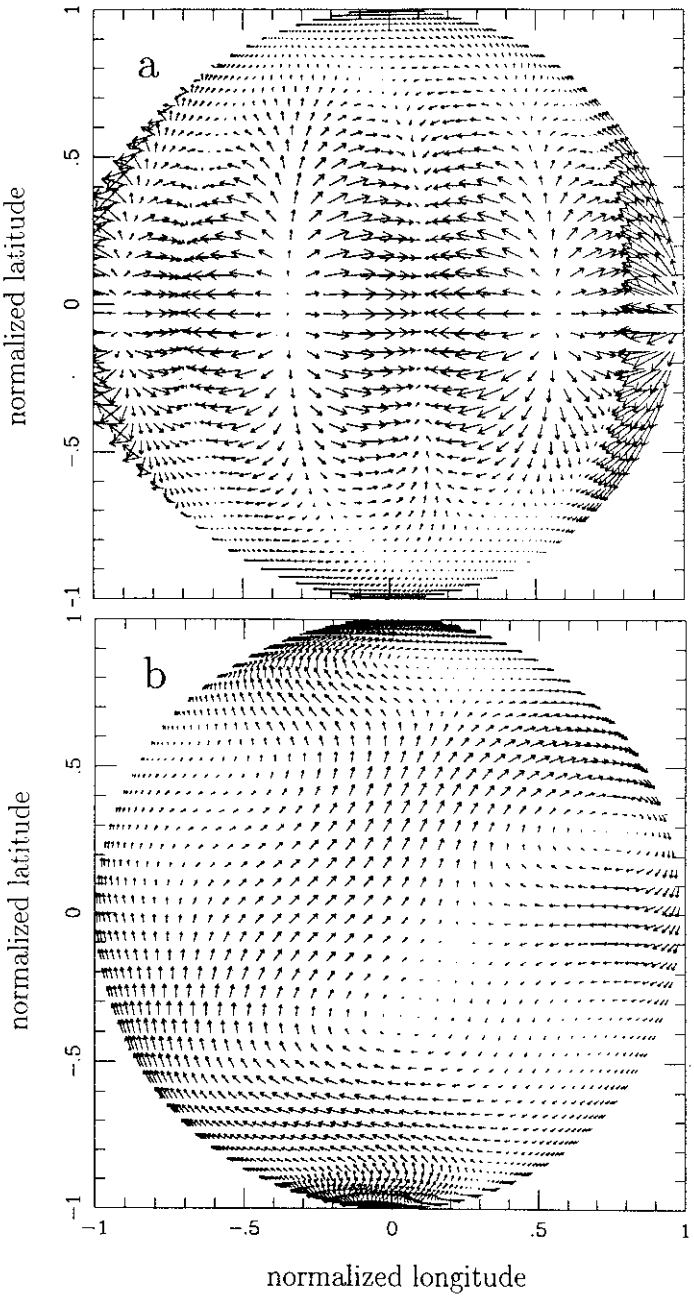

FIG. 2.—(*a*) Horizontal component of the poloidal flow field for $1 \le s \le 7$, odd s; $-s \le t \le s$ at radial level $r = 0.95\ R_\odot$. The latitude and longitude are normalized. The horizontal flow displays alternating zones of divergence and convergence corresponding to the well-known banana cells. (*b*) Toroidal flow field for $1 \le s \le 7$, odd s; $-s \le t \le s$ at radial level $r = 0.95\ R_\odot$. Streamlines are confined to spherical shells. In contrast to the poloidal flow plotted in (*a*), the toroidal field is divergence-free.

Because of their distinctive geometries, poloidal and toroidal flows affect acoustic modes in different ways. For example, under degenerate perturbation theory modal coupling is insensitive to the poloidal component of the flow and to the even-degree component of the toroidal flow (see Lavely & Ritzwoller 1992). Figures 2*a* and 2*b* are plots of the poloidal and toroidal velocity fields for a subset of the expansion coefficients. These figures illustrate the well-known facts that poloidal flows are characterized by zones of convergence and divergence, whereas toroidal flows are confined to spherical shells and have closed streamlines. We use degenerate perturbation theory in this paper, and, therefore, the poloidal component of the flow is not included in our calculation. Nonetheless, we have shown these coefficients to emphasize a fundamental nonuniqueness inherent in degenerate perturbation theory: the frequencies and displacement patterns of modes in the convecting model are insensitive to dynamically significant components of the flow.

2.2. *The Differential Rotation Model*

The velocity field due to differential rotation is the toroidal, odd-degree, axisymmetric component of the total velocity field $\boldsymbol{u}_0$, i.e., the terms $w_s^0(r)\hat{\boldsymbol{r}} \times \nabla_1 Y_s^0(\theta, \phi)$ for odd s. These are the same basis functions used by Ritzwoller & Lavely (1991) in their study of the forward and inverse problems of differential rotation. We replaced the low-degree components w_1^0, w_3^0, and w_5^0 of Glatzmaier's velocity model with components that reproduce the velocity field inverted from helioseismic data by Libbrecht et al. (1990). This change was made to make our simulations more realistic, since, as we show in § 5, coupling strength is a strong function of differential rotation. Inversions of helioseismic data (e.g., Libbrecht et al. 1990; Brown et al. 1989) suggest that the rotation profile is constant on concentric spheres, whereas Glatzmaier's differential rotation velocity field is constant on cylinders.

We have adopted $\Omega/2\pi = 400$ nHz as the value of the average angular surface rotation rate. Thus, in the corotating frame, the differential rotation profile of Libbrecht et al. (1990) (in radians per second) is given by

$$\Omega(r, \theta) = 2\pi \sum_{k=0,2,4} \Omega_k(r) \cos^k \theta\ , \tag{9}$$

where $\Omega_0 = 30$ *n*Hz, $\Omega_2 = \Omega_4 = 0$ for $0 \le r \le r_c$, and where $\Omega_0 = 62$ nHz, $\Omega_2 = -58$ nHz, $\Omega_4 = -84$ nHz for $r_c \le r \le R_\odot$, r_c being the radius at the base of the convection zone. The velocity field corresponding to the angular rotation rate in equation (9) can be expressed in terms of the toroidal, odd-degree, axisymmetric expansion coefficients of the vector spherical harmonics (Ritzwoller & Lavely 1991):

$$\frac{w_1^0(r)}{2\pi} = 2\sqrt{\frac{\pi}{3}}\, r\left[\Omega_0(r) + \frac{\Omega_2(r)}{5} + \frac{3\Omega_4(r)}{35}\right], \tag{10}$$

$$\frac{w_3^0(r)}{2\pi} = 2\sqrt{\frac{\pi}{7}}\, r\left[\frac{2\Omega_2(r)}{15} + \frac{28\Omega_4(r)}{315}\right], \tag{11}$$

$$\frac{w_5^0(r)}{2\pi} = 2\sqrt{\frac{\pi}{11}}\, r\left[\frac{8\Omega_4(r)}{315}\right]. \tag{12}$$

3. THE SPLITTING MATRIX

In this section we discuss the splitting matrix, $\mathbf{H}_k$, and its numerical computation using the convective model of Glatzmaier. The derivation of the splitting matrix is based on the assumptions that the convective flow field is steady state and anelastic, and that the governing equations of motion are linearizable in the mode displacement and convective flow field. Lavely & Ritzwoller (1992) discussed the significance of each assumption and argued that, with the exception of the steady state assumption, each is valid over the entire solar convection zone with the exception of a thin layer near the surface, constituting approximately 0.3% by radius of the convection zone, where the convection is highly turbulent. Since Glatzmaier's model does not extend this close to the surface, these assumptions are satisfied over the entire radial extent of Glatzmaier's model.

The only troubling assumption is that the convective flow field is steady state in the frame in which the perturbed equations of motion are solved. However, large-scale magnetic activity observed at the solar surface and large-scale numerical simulations such as those of Glatzmaier (1984) suggest that there are coherent flows at depth that are sustained from periods of time ranging from several weeks to several months. Furthermore, mixing-length calculations show that the lifetime of eddies near the base of the convection zone is approximately 1 month. (Fig. 1 of Lavely & Ritzwoller 1992 shows the characteristic convective time scales, length scales, and velocities predicted by mixing-length theory as a function of radius.) Thus, though solar convection is definitely not steady, long-wavelength components of the flow deep in the convection zone may be approximately steady over a single observing interval (1–3 months). Furthermore, a laboratory model of convection in a rotating shell operated in the microgravity environment of *Spacelab 3* (Hart et al. 1986a; Hart, Glatzmaier, & Toomre 1986b) showed sustained giant-cell features that are similar to those modeled by Glatzmaier. Therefore, Lavely & Ritzwoller (1992) suggested that their theory should be interpreted as a short-time approximation of a full theory governing nonsteady flows.

However, with respect to the results we wish to stress in this paper, the nonstationary nature of solar convection is not centrally important. We will show in § 5 that in the simulations reported here the most significant signature of convection is a systematic nearly m-parabolic line broadening due to modal coupling. The qualitative nature of this signature is not dependent on the stationarity of convection. Time-varying flows will produce the same helioseismic signature as a stationary flow, although the details of the coupling and, thus, the line widths and frequencies will change with time if the flow field is time-varying.

The major result of the theory of Lavely & Ritzwoller (1992) is a formal expression for the splitting matrix (their eq. [90]). The matrix element $H_{nl}^{m'm}$ describes the convective coupling of the SNRNMAIS modes (n, l, m) and (n, l, m') and depends on the radial eigenfunctions of these modes and on the expansion coefficients that characterize the convective flow field. The modes of a SNRNMAIS solar model may couple strongly in the presence of a convective flow provided that certain conditions are satisfied. These conditions are stated formally as selection rules in § 7 of Lavely & Ritzwoller (1992). Qualitatively put, the degree of coupling depends on the strength of the structural asphericity or convective field producing the coupling, the proximity of the eigenfrequencies of the modes, the relation between the geometries of the perturbing field and the oscillations, and the similarity of the radial eigenfunctions of the two modes. It was shown in Lavely & Ritzwoller (1992) that the strength of coupling varies as the square of the matrix element $H_{nl}^{m'm}$, and as the inverse of the difference $H_{nl}^{m'm'} - H_{nl}^{mm}$. The latter depends solely on the differential rotation, and, therefore, modal coupling strength is strongly controlled by the differential rotation. Modes that are most nearly degenerate couple the strongest. The frequencies used in assessing near-degeneracy should be taken in the corotating frame.

Practical use of the splitting matrix requires its eigenvalue-eigenvector decomposition:

$$\mathbf{\Lambda}^{(k)} = \mathbf{A}^{(k)\dagger} \mathbf{H}_k \mathbf{A}^{(k)} , \tag{13}$$

where $\mathbf{A}^{(k)}$ is the eigenvector matrix that diagonalizes $\mathbf{H}_k$ and $\mathbf{\Lambda}^{(k)}$ is the diagonal matrix containing the eigenvalues of $\mathbf{H}_k$. This result and the components $H_{nl}^{m'm}$ of the splitting matrix are presented in Appendix B. The expansion coefficients that define the eigenfunctions of the convecting model are given by the components of the eigenvectors of $\mathbf{H}_k$ such that the jth eigenfunction is written

$$u_k^j(r) = \sum_{m=-l}^{l} A_{mj}^{(k)} s_k^m(r) , \tag{14}$$

where the complex constants $A_{mj}^{(k)}$ $(-l \le m \le l)$ are the components of the jth eigenvector of the splitting matrix. The associated eigenfrequency of the jth eigenfunction is given by $\omega_k + \delta\omega_j$, where ω_k is the degenerate frequency, and $\delta\omega_j = \Lambda_{jj}^{(k)}$. We have labeled the row index of $A^{(k)}$ with the azimuthal order m (where the first row corresponds to $m = -l$), since the elements of the mth row specify the contributions of the spherical harmonic, Y_l^m, of the spatial filter to the $(2l + 1)$ eigenfunctions denoted by the j index.

The numerical computation of the splitting matrix and its eigenvalue-eigenvector decomposition represent the bulk of the computational labor. The radial integrals in the matrix elements $H_{nl}^{m'm}$ (eq. [B3]) are evaluated by computing the cubic spline fit to the integrands and performing the integration analytically. Recurrence relations for the Wigner 3-j symbols can be found in Schulten & Gordon (1975), and computational algorithms are included in Zare (1988). The splitting matrix is decomposed using the complex Hermitian path in EISPACK (Smith et al. 1976). It is only necessary to compute numerically the full upper triangle of the splitting matrix because of its Hermitian symmetry.

The radial expansion coefficients for the convective model were computed by Glatzmaier as a summation over Chebyshev polynomials for each degree and order. We interpolate these coefficients onto the radial knots of our spherical model. The splitting matrix, $\mathbf{H}_k$ (eq. [B3]), is then assembled using the toroidal velocity field expansion coefficients w_s^t in the range $1 \le s \le 30$; $-s \le t \le s$, and its eigenvalues and eigenvectors are computed. The multiplets ${}_nS_l$ used here lie in the range $5 \le l \le 95$, and the range of n for each l corresponds to the modes that have been observed by Libbrecht et al. (1990).

To gauge which modes should couple strongly for the convection model described in § 2.1, we consider the frequency splitting generated by the axisymmetric component of the model. In particular, we plot in Figure 3 the frequency splitting of the multiplet ${}_{10}S_{42}$, which is representative of the frequency splitting of all the multiplets considered here. The complete

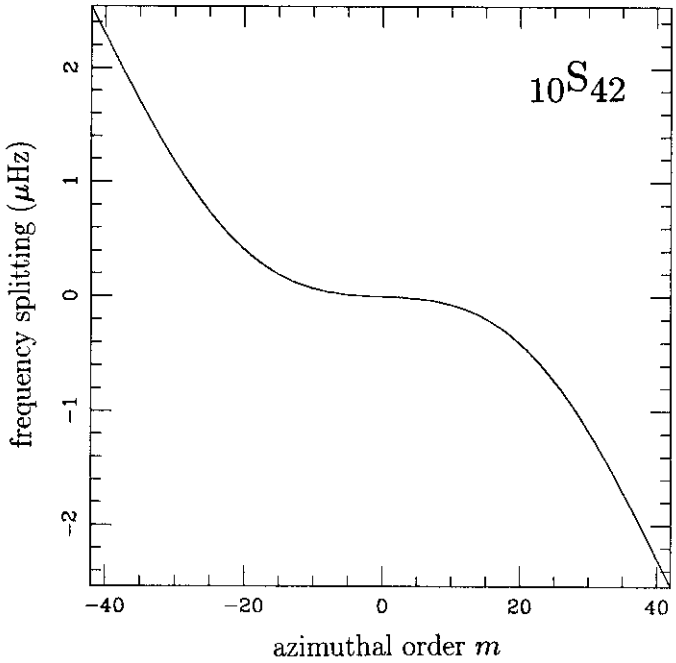

FIG. 3.—Frequency splitting produced by the differential rotation model described in § 2.2 in the corotating frame for the multiplet ${}_{10}S_{42}$. Frequency splitting in the nonaxisymmetric convective model described in § 2.1 remains dominated by the differential rotation. Modes that are most nearly degenerate in frequency tend to couple most strongly. Thus, the presence of a plateau in the frequency splitting for low-$|m|/l$ states suggests that the coupling strength will be greatest among SNRNMAIS modes with low $|m|/l$ values.

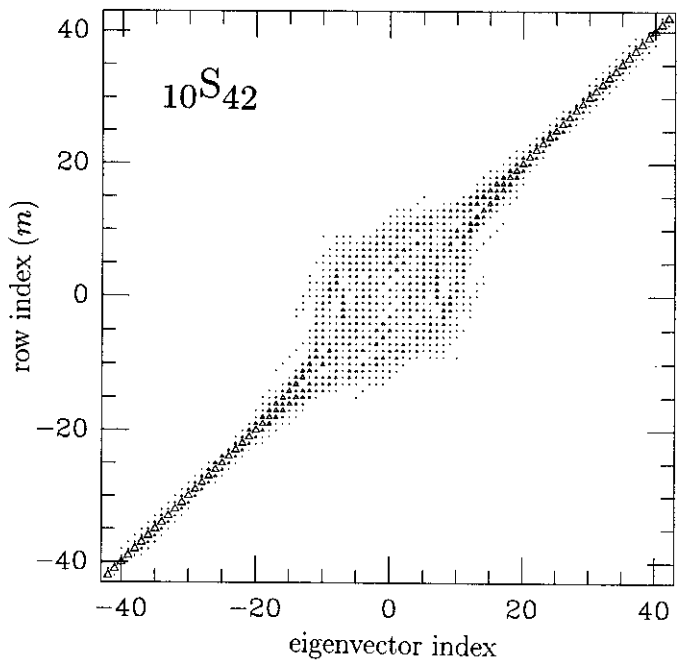

FIG. 4.—Moduli $|A^{(k)}_{mj}|$ of the complex eigenvector components of the eigenvector matrix for the multiplet ${}_{10}S_{42}$. Each column contains the modulus of the coefficient in the eigenfunction expansion for the displacement pattern of a mode of the convecting solar model (see eq. [14]). Each row corresponds to a unique value of m of a SNRNMAIS eigenfunction. The rows are arranged from top to bottom in order of increasing m (the top and bottom rows correspond, respectively, to $m = -l$ and $m = l$). The eigenvectors are arranged in equidistant increments from left to right in order of decreasing (associated) eigenfrequency. In a purely axisymmetric solar model, the only nonzero components of the eigenvector matrix would be along the diagonal, and each eigenvector could be uniquely identified with a single m-state given by the indices on the horizontal axis. It is evident that coupling strength is greatest among the low-$|m|/l$ states.

differential rotation model is prescribed by the axisymmetric component of the toroidal velocity field expansion coefficients $[w^0_s(r),\ 1 \le s \le 30;\ \text{odd } s]$. The frequencies were calculated with equation (B6). They are transformed to the inertial frame by the substitution $\omega^m_k \to \omega^m_k - m\Omega$, as discussed in Appendix C1. The most prominent feature of the splitting profile is the broad plateau for low-$|m|$ states where the frequency difference $\omega^m_k - \omega^{m\pm1}_k$ is much smaller than the corresponding difference for high-$|m|/l$ states. Thus, low-$|m|$ modes in the SNRNMAIS solar model will couple more strongly in the presence of nonaxisymmetric convection than high-$|m|/l$ modes.

Another way to assess the strength of coupling is by inspection of the eigenvector matrix $\mathbf{A}^{(k)}$ (defined by eq. [B1]). Figure 4 shows the moduli of the eigenvector components $A^{(k)}_{mj}$ of the multiplet ${}_{10}S_{42}$. The eigenvectors are plotted in order of decreasing eigenfrequency, and are arranged in equidistant increments along the horizontal axis. For a spherical or axisymmetric solar model, each mode of oscillation is uniquely identified with a single spherical harmonic so that the eigenvector matrix is diagonal, i.e., the only nonvanishing components of the eigenvector matrix are given by $A^{(k)}_{mm}$ for $-l \le m \le l$. Since modal frequencies of the convecting model are dominated by differential rotation, we can associate an eigenvector of the convecting model with the corresponding single-component eigenvector of the axisymmetric model. Figure 4 shows that the greatest hybridization (coupling of m-states) is among those modes that are identified with low-$|m|$ states in the axisymmetric or differentially rotating model. This is in accordance with the near-degeneracy of these modes (see Fig. 3). The eigenvector matrix for the multiplet ${}_{10}S_{42}$ is plotted in Figure 5 with the eigenvectors arranged along the horizontal axis according to their associated eigenfrequencies. The height of the spikes in each row of this figure is proportional to the moduli of the eigenvector components. The strong frequency dependence of the spike density emphasizes the dependence of coupling strength on near-degeneracy. This effect is what leads to the systematic line broadening discussed in § 5 that is the hallmark of large-scale convection.

4. POWER SPECTRA AND SPECTRAL ESTIMATION IN THE ENSEMBLE AVERAGE

It is worthwhile to note the distinction between the eigenvalues of $\mathbf{H}_k$ (which determine the modal frequencies of the convecting model) and the frequencies estimated from helioseismic time series. A modal frequency ω_j is the frequency of oscillation of the complex displacement pattern described by $\boldsymbol{u}^j_k(r)$. It is shown in Appendix D that the generalized resonance function that is retrieved from the spatial filtering process yields an apparent frequency that is a linear combination of the $(2l + 1)$ modal frequencies. We wish here to obtain expressions for the frequency and Q of the generalized resonance functions in the ensemble average. Most of the technical details relevant to this section are presented in Appendix C.

4.1. *Generalized Resonance Functions in the Ensemble Average*

Helioseismic displacement fields are observed from the surface of the Earth, and, therefore, for the results of this paper to be useful, the displacement field in equation (1) must be transformed to the observer's frame. This transformation is

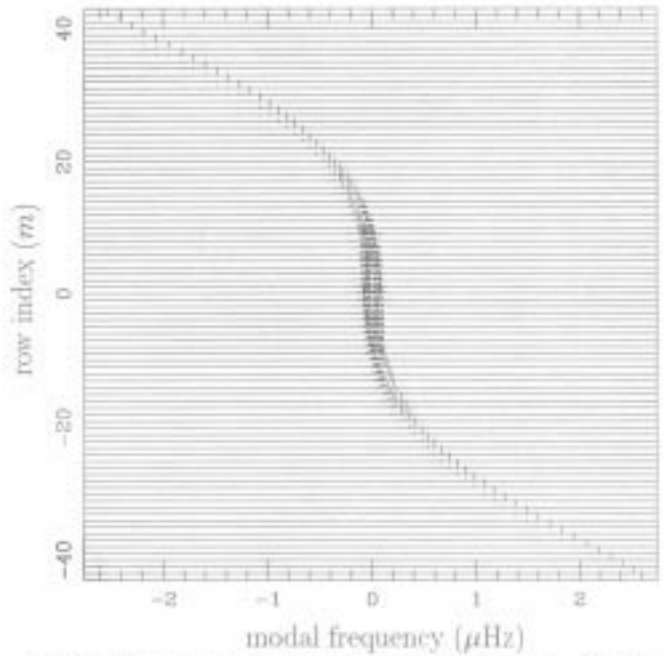

FIG. 5.—Modulus of the eigenvector matrix for the multiplet ${}_{10}S_{42}$, where each eigenvector is arranged on the horizontal axis according to its corresponding eigenfrequency in the corotating frame (with the degenerate frequency removed). The horizontal axis is in units of microhertz. The height of each spike is proportional to the modulus $|A_m^{(k)}|$ of the corresponding eigenvector component. The strong coupling for low-$|m|/l$ states results in an effective broadening of the frequency range over which each apparent m-state is nonzero. This variation of coupling strength with m yields the systematic m-dependent line broadening which is the hallmark of large-scale convection.

discussed in § C1. In § C2 we use this result to present an expression for the time series $F_k^{m'}(t)$ and power spectrum $|F_k^{m'}(\omega)|^2$ associated with the $Y_l^{m'}$ component of the acoustic displacement field of the multiplet ${}_nS_l$. We find that $|F_k^{m'}(\omega)|^2$ can be written

$$|F_k^{m'}(\omega)|^2 = {}_nU_l^2\omega^2 \sum_{j=-l}^{l} \sum_{j'=-l}^{l} A_{m'j}^{(k)} A_{m'j'}^{(k)*} \sum_{i=-l}^{l} \sum_{i'=-l}^{l} A_{ji}^{(k)\dagger} A_{j'i'}^{(k)*\dagger} \times \sum_{\sigma} \sum_{\sigma'} a_i^{\sigma,k}(\omega) a_{i'}^{\sigma',k*}(\omega) \lambda_{m'j}^{(k)}(\omega) \lambda_{m'j'}^{(k)*}(\omega) . \quad (15)$$

We use two assumptions to simplify equation (15). The first asserts the equipartition of energy among the $(2l + 1)$ m-states of a given multiplet. That is, the expected value of the modulus of $\sum_{\sigma'} a_m^{\sigma,k}(\omega)$ (where the sum is over all σ) is independent of m. This assumption is based on the prevailing conception that the sources of acoustic energy in the Sun are uncorrelated and isotropically distributed and is, more importantly, justified by observation (e.g., Libbrecht et al. 1990). The second is the random-phase approximation, which is stated mathematically in its application to the source coefficients by equation (C9). It removes one of the summations over σ in equation (15). Using these assumptions and the unitarity property of the eigenvector matrix, $\mathbf{A}^{(k)}$, we show in § C3 that the power spectrum in the ensemble average of the multiplet ${}_nS_l$ with spatial shape given by the spherical harmonic component $Y_l^{m'}$ is given by

$$|F_k^{m'}(\omega)|^2 = \frac{{}_nU_l^2\omega^2|b_k(\omega)|^2}{4} \sum_{j=-l}^{l} \frac{|A_{m'j}^{(k)}|^2}{\alpha_k^2 + (\omega - \omega_{jk}^{m'})^2} , \quad (16)$$

where

$$|b_k(\omega)|^2 = \sum_{\sigma} |a_{m'}^{\sigma,k}(\omega)|^2 \quad \text{for} \quad -l \le m' \le l . \quad (17)$$

We call $|b_k(\omega)|^2$ the *source spectrum*. Since the source spectrum for any given realization is unknown, the estimation of the line width and frequency of $|F_k^{m'}(\omega)|^2$ is compromised. As discussed by Kelly & Ritzwoller (1993), the source spectrum presents multiplicative noise through which we must attempt to estimate the spectral characteristics. For this reason we consider below the statistical properties of $|F_k^{m'}(\omega)|^2$ in the ensemble average over many realizations of the source process.

In any single realization, $|b_k(\omega)|^2$ will be a stochastic function of frequency. By the energy equipartition assumption, the expected value of the source spectrum is constant over the narrow frequency range spanned by the multiplet. Therefore, the source spectrum is locally flat in the ensemble average. The ensemble average (denoted by angular brackets) of the source spectrum then is just

$$\langle |b_k(\omega)|^2 \rangle = |b_k|^2 , \quad (18)$$

where $|b_k|$ is the expected value of the source spectrum in the narrow frequency band around multiplet k. It is interesting to note that a flat source spectrum is identical to a source time history given by a temporal delta function. The ensemble-average power spectrum can now be written as follows:

$$\langle |F_k^{m'}(\omega)|^2 \rangle = \frac{{}_nU_l^2\omega^2|b_k|^2}{4} \sum_{j=-l}^{l} \frac{|A_{m'j}^{(k)}|^2}{\alpha_k^2 + (\omega - \omega_{jk}^{m'})^2} . \quad (19)$$

Equation (19) is the central analytical result of this paper and will be used to estimate the frequencies and line widths of the resonance function associated with the spherical harmonic $Y_l^{m'}$. We refer to $\langle |F_k^{m'}(\omega)|^2 \rangle$ as the *power spectrum of the generalized resonance function in the ensemble average*.

4.2. *Spectral Analysis of the Generalized Resonance Function in the Ensemble Average*

Most helioseismological inferences are based upon measurements of the frequencies, line widths, and amplitudes of observed spectra. These data are functionals of the structure and dynamics of the Sun. The resonance function for a convecting model in the ensemble average (eq. [19]) is our synthetic datum here and forms the basis of our data analysis. The methods we use to assign a frequency and line width to this resonance function are described in Appendix D.

The frequencies, line widths, and amplitudes of generalized resonance functions are not precisely defined, since there is no simple analytic function that exactly models the frequency dependence of the resonance functions. This has motivated our use of the terms *apparent frequency* and *apparent Q*, ω_{app} and Q_{app}, respectively. However, Lorentzians can approximately model the properties of generalized resonance functions, with the disadvantage that the model cannot exactly fit even noise-free data and the estimated parameters that characterize the Lorentzian depend on the fitting technique. Lorentzian fitting schemes commonly used to estimate these parameters include least-squares fitting (Masters & Gilbert 1983), the full width at half-maximum (FWHM) method, and algebraic weighting techniques (Dahlen 1979). Since each fitting scheme magnifies departures from Lorentzian behavior differently, the resulting frequency and line-width estimates from each differ. In general, the residual between the model Lorentzian and actual spectrum varies as a function of frequency and m-state. The dependence on the m-state follows from the asymmetry of the eigenvector matrix as a function of row index (each row is identified with a single m-state). Further, the residual is a function of the fitting procedure. For example, the FWHM method

depends only on two points of the spectrum, whereas the least-squares method depends on the entire spectrum over which the fitting is performed. Of course, these methods yield the same estimate of the line width if the spectrum is a perfect Lorentzian, but they may yield quite different results if, for example, the power of the spectrum away from the half-maximum points is significantly different from a Lorentzian spectrum. That this effect is a function of the m-state can be seen from the components of the eigenvector matrix shown in Figure 5 and from the discussion in § 5.

To illustrate the non-Lorentzian character of generalized resonance functions, we have plotted $\langle |F_k^0(\omega)|^2 \rangle$ (eq. [19]) in Figure 6 for the convecting and differentially rotating models as well as the Lorentzian that approximates the resonance function of the convecting model. This figure shows the most important effect of convection, the convective line broadening, and it also illustrates the departure from Lorentzian behavior. Nonetheless, we have chosen to model generalized resonance functions as though they were Lorentzians, i.e., we characterize each resonance function by its amplitude, half-width, and frequency centroid, and use first-moment and FWHM fitting procedures as they are applied to Lorentzians. We use these methods, since they are easy to perform; Kelly & Ritzwoller (1993) present methods designed for use on real data.

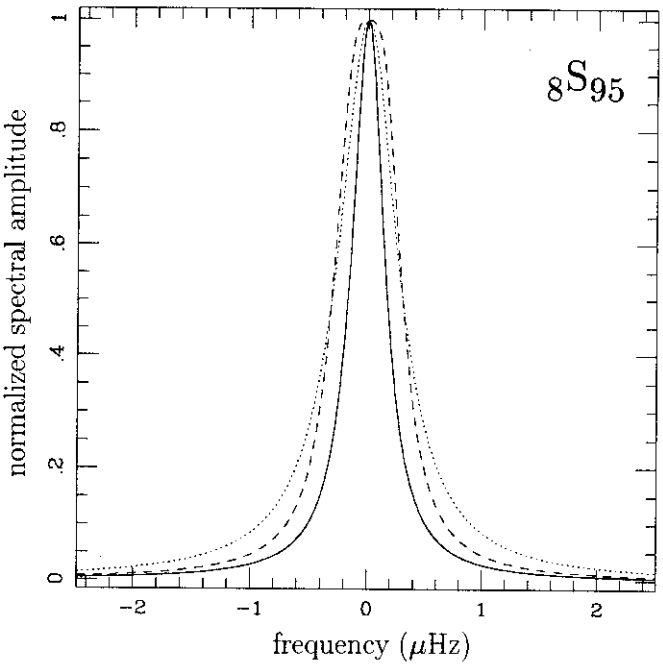

FIG. 6.—Three power spectra of the apparent $m = 0$ state of the multiplet $_8S_{95}$. The solid line is a perfect Lorentzian and is the power spectrum produced by the axisymmetric differentially rotating model of § 2.2. The dotted line is the ensemble-average power spectrum produced by the odd-degree toroidal component of the convective model described in § 2.1 for $1 \leq s \leq 30$ and $-s \leq t \leq s$. This spectrum is a sum of Lorentzians computed with eq. (19). The FWHM-estimated Lorentzian which approximates the generalized resonance function of the convecting model is given by the dashed line. This figure illustrates that large-scale convection generates non-Lorentzian spectra, and that spectral lines are broadened relative to the resonance function of the differentially rotating model. Nevertheless, the spectrum is Lorentzian-like, and we are motivated to fit the spectra of the convecting model with Lorentzian functions. The intrinsic quality factor of the axisymmetric model and of each of the Lorentzians that contribute to the sum in the ensemble average for the convecting model are given by 10^4. The estimated apparent quality factor of the model Lorentzian is 5569.

The large quantity of helioseismic data has led observers to parameterize their data in simple functional forms. In keeping with this practice, we parameterize apparent frequencies within a multiplet in the form

$$\omega^m_{k,\mathrm{app}} = \omega_k + l \sum_{j\,\mathrm{odd}} a^k_j P_j(-m/l)\,, \tag{20}$$

where P_j is the degree-j Legendre polynomial. Since frequency splittings are antisymmetric in m about the degenerate frequency, only odd terms need be retained in the sum. (See Fig. 4 in Lavely & Ritzwoller 1992.) We truncate the series at $j = 5$ here. Ritzwoller & Lavely (1991) argued that, in spite of its wide usage in the helioseismological community, this parameterization is a suboptimal representation of splitting data, especially for the purpose of inversion for differential rotation, and that Clebsch-Gordan coefficients should be used instead of Legendre polynomials. Nonetheless, in § 5 we summarize the results of our synthetic splitting experiments in terms of the a^k_j coefficients to facilitate comparison with observed a^k_j coefficients. In analogy with equation (20), we introduce the following expansion for the m dependence of the apparent quality factor $Q^m_{k,\mathrm{app}}$:

$$Q^m_{k,\mathrm{app}} = q^k_0 + \sum_{j\,\mathrm{even}} q^k_j P_j(m/l)\,. \tag{21}$$

However, we have not included a factor of l in the definition of $Q^m_{k,\mathrm{app}}$ since, unlike the frequency splittings, the apparent quality factors do not show a dominantly linear dependence on l. Since apparent Q variations are symmetric in m, only even terms need be retained in the sum. Note that, in contrast to geophysical applications, here $q \neq Q^{-1}$. In the simulations presented here, only two terms will need to be retained, q^k_0 and q^k_2.

5. NUMERICAL ESTIMATES OF APPARENT FREQUENCIES AND LINE WIDTHS

In this section we present the two most important results of the paper. First, we show that large-scale convection can significantly and systematically broaden resonant lines. The characteristic line-broadening pattern is strongly dependent on the apparent m-state, with low-$|m|/l$ states the most significantly broadened (which follows from their near-degeneracy). This line broadening is dominantly parabolic in m for Glatzmaier's model. Second, frequency perturbations produced by Glatzmaier's convective model are at or below the current noise level of observations. In §§ 5.1 and 5.2, we describe the effect of convection on frequencies and line widths, respectively. In § 6 we discuss, among other things, the observed properties of helioseismic oscillations that are suggestive of the convective line-broadening effect.

Lavely & Ritzwoller (1992) discussed in detail how the frequency degeneracy of a given multiplet is lifted by the advective effect of convection and differential rotation, although differential rotation dominates the frequency splitting for the models considered here. For an axisymmetric flow, the perturbation in phase velocity is greater for a wave propagating in the direction of the flow than for a wave propagating obliquely to the flow. This effect is illustrated from a modal-theoretic viewpoint in Figure 3. Waves associated with the azimuthal orders $m = \pm l$ travel directly with or against the axisymmetric flow field and, consequently, display the largest frequency perturbations, whereas the $m = 0$ wave propagates along the

polar great-circle path so that its frequency perturbation is zero. Analogous interpretations for a convecting model are more complicated, as can be seen in Figure 2*b*, which shows the nonaxisymmetric component of the odd-degree toroidal flow to degree $s = 7$. In the traveling wave representation, a wave whose wavevector is initially inclined at a given angle with respect to the rotation axis is continuously deflected from a great-circle path by the nonaxisymmetric velocity field. The resulting wave requires a sum of spherical harmonic basis functions (the eigenfunctions of the SNRNMAIS model) to represent its path. This is modal coupling. Thus, modes in this model cannot be identified with a single spherical harmonic. For a nonaxisymmetric flow, the notion of a wave propagating along a fixed great circle breaks down. Instead, the wave front must be represented with a linear combination of spherical harmonics, and the expansion coefficients are given by the column vectors of an eigenvector matrix such as the matrices displayed in Figures 4 and 5. The interpretation of a mode identified with a single m-state and great-circle propagation path is approximately valid if a single component in a given eigenvector dominates all other components.

We show in this section that the dominant way in which convection manifests itself in helioseismic data is in terms of modal line widths rather than frequencies. The estimation of both modal line widths and frequencies requires the use of equation (19) to compute the ensemble-average spectrum, $\langle |F_k^{m'}(\omega)|^2 \rangle$. This requires the construction and decomposition of each splitting matrix as described in § 3. Each generalized resonance function is computed over a 15 μHz interval centered about the frequency $(\omega_k - m'\Omega)$ with a frequency binning of 0.035 μHz. The apparent frequency of each resonance function is estimated according to the procedures described in Appendix D. We evaluated the moment integral in equation (D2) with a Newton-Cotes quadrature scheme, and we implemented the weighted-sum method in equation (D3). The agreement that was found between these estimates served as a consistency check. The splitting coefficients a_j^k (eq. [20]) for $1 \le j \le 5$ were then obtained from the estimated frequencies $\omega_{k,\mathrm{app}}^{m'}$ $(-l \le m' \le l)$ by linear regression. Two sets of coefficients were calculated, one each corresponding to the convecting and differentially rotating models described in § 2.

Estimation of line widths is more troublesome, since the values obtained are dependent on the nature of the estimator. In this paper, for simplicity, we use the FWHM method described in Appendix D to estimate line widths, and, subsequently, apparent quality factors $Q_{k,\mathrm{app}}^m$. The synthetic generalized resonance function was computed for an infinite-length, untapered time series, and so we use equation (D6) with $T = \infty$ to estimate line widths. However, as discussed by Kelly & Ritzwoller (1993), this method is not successful in retrieving useful Q measurements with realistic data. They discuss a least-squares fitting procedure that does work. Since the FWHM method produces fits that intersect the input generalized resonance function at the half-maximum point, and since the least-squares result tends to cross the input function above this point, least-squares Q estimates tend to be smaller than the FWHM estimates. Consequently, the ensemble-average Q-values presented in this paper will be larger than in our subsequent papers, and the variation of apparent Q within a multiplet will be smaller. The FWHM estimated line widths are used to calculate apparent quality factors, and these are exposed in terms of the expansion coefficients, q_0^k and q_2^k, defined by equation (21).

5.1. *The Effect of Convection on Estimated Helioseismic Frequencies*

A useful way to assess the effect of convection on frequencies is to compare frequencies associated with a single spherical harmonic displacement pattern in the convecting and differentially rotating models. As an example, we plot in Figure 7 the residual in apparent frequency between the convecting and differentially rotating models described in § 2 for the multiplet ${}_8S_{95}$. The residual pattern is a characteristic feature of splitting for the multiplets considered here. Systematic behavior of frequency splitting for different multiplets k is mirrored in the systematic behavior of the a_j^k expansion coefficients. We have plotted in Figures 8*a*–8*c* the residuals of these coefficients between the convecting model and its axisymmetric counterpart for the harmonic degrees $j = 1$, $j = 3$, and $j = 5$, respectively. Standard deviations of the model parameters have been estimated by assuming that the errors of the frequency estimates represent a Gaussian process with values given by the difference between the input frequencies and the truncated Legendre polynomial fit to the frequencies. The errors would be zero if sufficient Legendre polynomials were included to fit the data perfectly. The standard deviations are nonzero, since there exists structure in the frequency splittings higher than degree 5. The standard deviations of the estimated splitting coefficients a_1^k and a_3^k are typically small relative to the differences of these coefficients for the convecting and differentially rotating models. However, the difference in the a_5^k coefficients between the two models is generally comparable to the standard deviation of the estimated a_5^k of the convecting model.

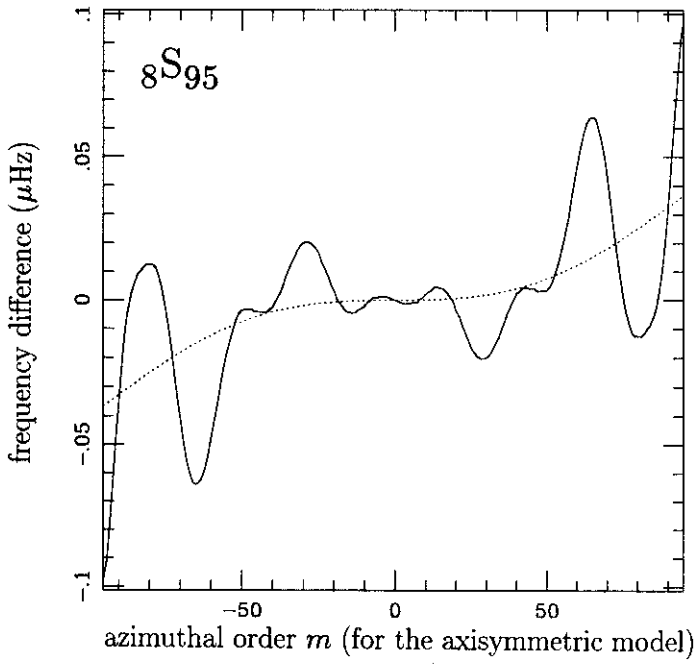

FIG. 7.—The solid line is the difference (or residual) in the estimated apparent frequency, $\omega_{k,\mathrm{app}}^m$, of the multiplet ${}_8S_{95}$ between two models: the differential rotation model described in § 2.2 and the odd-degree toroidal component of velocity field model described in § 2.1, which is just the flow represented by the coefficients w_s^t for $1 \le s \le 30$, odd s, and $-s \le t \le s$. The dotted line is the difference between the Legendre polynomials fitted to the velocities of the differentially rotating and convecting models, where each series is truncated at degree $N = 5$ (see eq. [20]). Note the odd symmetry of the split frequencies. This figure illustrates the failure of the low-degree polynomial fit to capture the frequency residuals, which are peaked near the sectoral modes.

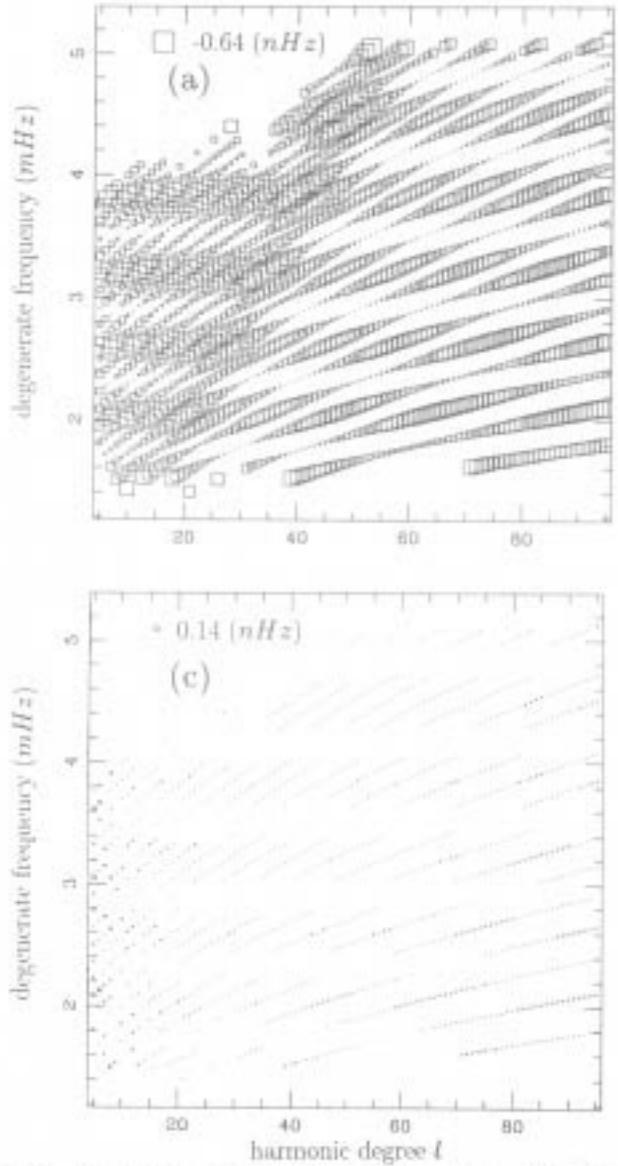

FIG. 8.—Differences (in nanohertz) of the splitting coefficients a_j^k defined by eq. (20) for the convecting model and a_j^k for the differentially rotating velocity model for (*a*) $j = 1$, (*b*) $j = 3$, and (*c*) $j = 5$. (That is, $a_j^{k,\text{conv}} - a_j^{k,\text{d.r.}}$.) The size of each symbol is proportional to the magnitude of the frequency difference, and the size normalization is constant across the three plots. The largest differences for the $j = 1$, 2, and 3 coefficients are 0.64 ($_{18}S_{4\nu}$), 0.27 ($_3S_{9\nu}$), and 0.14 ($_{16}S_{3\nu}$) nHz, respectively. The coefficients tend to increase with increasing l and display zones of extinction as a function of the degenerate frequency of the multiplets. This extinction takes place at frequencies where the toroidal sensitivity kernels of the multiplets become nearly orthogonal with the radial variation of the velocity model. Consequently, their location is a strong function of the convective flow field. The a_1 coefficients also display a maximum at an angle of about 60° with the horizontal in (*a*). These are the modes that bottom near the base of the convection zone. Error estimates caused by the misfit due to series truncation at $N = 5$ for the $j = 5$ coefficients are at or below the noise level, which explains the randomization of symbol size for the a_5 coefficients at low l.

Typical values of a_1^k, a_3^k, and a_5^k are, respectively, 400, 20, and 5 nHz. It is evident from Figures 8*a*–8*c* that differences in like-degree splitting coefficients of the two models are relatively small. Indeed, comparison of the splitting coefficient differences with the error estimates of the corresponding observed splitting parameters in Libbrecht et al. (1990) shows that the frequency signal produced by Glatzmaier's model of nonaxisymmetric convection is well below the current level of observability.

The ability to detect the presence of large-scale convective flows through frequency measurements is dependent on a number of factors, including the size of the frequency perturbation, the coherence of the perturbation as a function of the m-state within each multiplet, and the coherence as a function of the multiplet index k. The splitting coefficient residuals between the convecting and differentially rotating models in Figures 8*a*–8*c* display systematic patterns as a function of the multiplet index. It is evident that the residuals are strongly frequency-dependent in that there are alternating zones of large and small residuals. This behavior can be understood by noting that the eigenfunction shapes are themselves strongly frequency-dependent (see, for example, Figs. 3*a* and 3*b* of Lavely & Ritzwoller 1992, which show the radial dependence of the eigenfunctions of near-degenerate modes). The zones of extinction correspond to near-orthogonality of the velocity model with the eigenfunction shapes. The residuals of the a_1^k splitting coefficients also display a maximum at an angle of approximately 60° with the horizontal. This maximum results from the fact that modes along this line bottom near the base of the convection zone and receive the greatest splitting effect.

Our results show that if the large-scale convective velocity field in the Sun is similar to Glatzmaier's model, then inversions for the differential rotation profile that use frequency splittings of low-l ($l < 100$) multiplets of the Sun are unlikely to be biased by global-scale convection. Similarly, searches for global-scale convection through measurements of apparent frequencies will be hampered by the small signal. However, the frequency perturbations presented here probably underpredict actual convection-caused frequency perturbations, since the upper radius of the numerical convection model is $\sim 0.95\ R_\odot$, which excludes the very large velocities that are expected in the top 15% of the convection zone. In addition, as seen in Figure 7, the representation of perturbed frequencies in terms of low-degree splitting coefficients fails to extract the largest frequency effects. This finding suggests the need for observers to obtain higher degree splitting coefficients, or at least to concentrate on nearly sectoral lines in searching for a giant-cell effect on frequencies. The stronger frequency perturbations of the high-m

states relative to the low-m states can be understood as follows. The low-m states contain frequency contributions from modes of the convecting model that are nearly similar in frequency, whereas the high-m states contain contributions from modes with larger frequency spreads whose contributions are less symmetric about the target m-state.

5.2. *The Effect of Convection on Estimated Helioseismic Line Widths*

5.2.1. *Interpretation of Line Widths in a Convecting Model*

It is customary to interpret modal line widths in terms of intrinsic damping processes. Several of the approaches that have been used are summarized in Christensen-Dalsgaard et al. (1989), who adopted the hypothesis that the acoustic modes are intrinsically damped but excited stochastically by convection. An oscillator that satisfies these conditions is modeled by a simple differential equation of the form

$$\frac{d^2A}{dt^2} + 2\alpha \frac{dA}{dt} + \omega_0^2 A = f(t) , \tag{22}$$

where $A(t)$ is the amplitude of a damped linear oscillator, α is the intrinsic damping rate, and $f(t)$ is a stationary random function. Christensen-Dalsgaard et al. (1989) showed that the average power spectrum of $A(t)$ is given by

$$\langle |A(\omega)|^2 \rangle = \frac{1}{4\omega_0^2} \frac{\langle |f(\omega_0)|^2 \rangle}{\alpha^2 + (\omega - \omega_0)^2} , \tag{23}$$

where the angle brackets denote the ensemble average, and it was assumed that $\langle |f(\omega)|^2 \rangle$ varies slowly with ω_0. From this result Christensen-Dalsgaard et al. (1989) concluded that it was appropriate to interpret line widths of a stochastically excited oscillator in terms of intrinsic damping.

Equation (23) is consistent with our equation (19) in that the spectrum is given by the product of a frequency-dependent function that is dependent on the nature of the source process and a Lorentzian whose half-width at half-maximum is related to the intrinsic damping of the medium, which we represent by α. However, the derivation of equation (23) did not account for the effect of modal coupling on the broadening of the width of the generalized resonance function produced by spatial filtering. When this effect is included, the power spectrum analogous to $\langle |A(\omega)|^2 \rangle$ and produced by the $Y_l^{m'}$ component of the time derivative of the acoustic displacement field is given by $\langle |F_k^{m'}|^2 \rangle$ in equation (19). [Note that eqs. (19) and (23) appear to differ by a factor of ω^4. One factor of ω^2 results from the fact that eq. (19) represents the spectrum of a velocity field, whereas eq. (23) is for the spectrum of a displacement field. The other factor of ω^2 comes from the definition of the source spectrum $b(\omega)$ in eq. (3).] It is evident that $\langle |F_k^{m'}|^2 \rangle$ is a linear combination of functions of the form $\langle |A(\omega)|^2 \rangle$, each with a different center frequency. Therefore, as will be discussed further in § 6, convective apparent line-broadening effects must be considered in the interpretation of observed line widths.

In equation (1), we assumed that the intrinsic attenuation rate of each mode is given by $\alpha_k = \omega_k/(2Q_k)$, where Q_k is the intrinsic quality factor associated with the multiplet ${}_nS_l$. Mechanisms of p-mode damping that contribute to line widths include, for example, radiative damping, turbulent viscosity, and nonlinear interaction with convection. Each of these mechanisms operates most effectively in a thin layer near the solar surface. Since eigenfunction shapes in the upper part of the convection zone are strongly frequency-dependent (see, for example, the eigenfunction plots in Figs. 3*a* and 3*b* of Lavely & Ritzwoller 1992), the intrinsic damping rates are also strong functions of frequency but are independent of the modal azimuthal order. Therefore, we have taken Q_k to be the same for all $(2l + 1)$ m-states associated with each multiplet. Although it is known that intrinsic quality factors strongly decrease with increasing degenerate frequency, as discussed earlier, for simplicity of presentation many of the results presented in the following section are computed with the assumption that the intrinsic quality factor is identical for all multiplets. In particular, we use $Q_k = 10^4$.

5.2.2. *Numerical Estimates of the Effect of Convection on Line Widths*

We wish to determine the nature of the convective line broadening witnessed, for example, in Figure 6, and to attempt to estimate the size of the effect that might be expected for the Sun. The cause of the line-broadening effect of convection can be seen in Figures 5 and 9. Figure 5 shows the modulus of the eigenvector components for the splitting matrix of ${}_{10}S_{42}$ plotted as a function of the frequency perturbation associated with each eigenvector matrix element. It demonstrates that coupling is strongest among nearly degenerate states, which correspond to the low-$|m|/l$ states for each multiplet. Figure 9 plots two generalized resonance functions for the $m = 0$ and $m = -61$ states of ${}_3S_{61}$ along with the eigenvector components and the Lorentzian fit. This figure clearly shows that line broadening results from modal coupling and is greatest where the coupling is greatest; i.e., for low-$|m|/l$ states. Thus, convection does not merely broaden spatially filtered spectral lines; it imparts a systematic line broadening, which is greatest near $m = 0$ and decreases (with small undulations) with increasing $|m|$. As we will show, the magnitude of the line broadening is a strong function of the intrinsic damping rate; the effect is negligible if the natural line width is greater than the convective line-broadening effect. In addition, the effect also strongly depends on the value of the harmonic degree l of the multiplet. As l increases, more SNRNMAIS modes are available for coupling, which results in a greater frequency spread of the contributors to the generalized resonance function of the apparent m-state. We will investigate here the pattern as functions of m, l, and ω, as well as the magnitude of the convective line broadening as a function of intrinsic Q_k.

Figures 10*a* and 10*b* show, respectively, the apparent quality factor estimates, for the multiplets ${}_3S_{61}$ and ${}_{17}S_{61}$, for five different values of the intrinsic quality factor Q_k, ranging from 2×10^3 to 10^4 in increments of 2×10^3. The convective line broadening is greatest for those multiplets with narrow natural line widths and, therefore, convective line broadening increases with increasing Q_k. The jagged behavior of $Q_{k,\mathrm{app}}^m$ with m in Figures 10*a* and 10*b* results from the asymmetry about the antidiagonal for a given row of the eigenvector matrix. Its exact form is a function of the line-width estimator, consistent with our discussion in § 4. The middle row of each eigenvector matrix, for example in Figure 4, corresponds to the $m = 0$ state of the spatial filter. Because of its symmetry it is the only row that generates a generalized resonance function symmetric about the frequency centroid. Other rows corresponding to other m-states produce skewed spectra because of departures of symmetry about the antidiagonal of the eigenvector matrix. The m-dependence of apparent Q, $Q_{k,\mathrm{app}}^m$, for each value of Q_k in Figures 10*a* and 10*b* is dominantly parabolic, consistent with

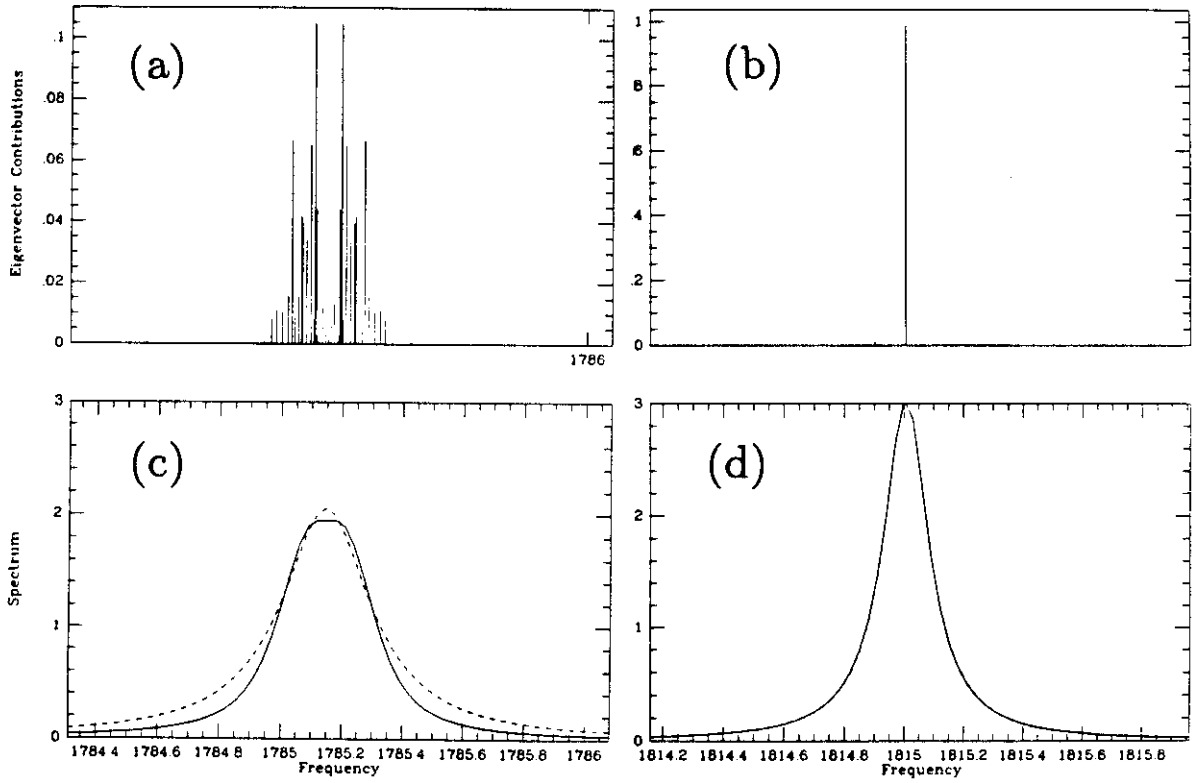

FIG. 9.—Plot of two rows of the eigenvector matrix for ${}_3S_{61}$ for (*a*) $m = 0$ and (*b*) $m = -61$ and the corresponding generalized resonance functions, (*c*) and (*d*). The generalized resonance functions are shown with a solid line, and the best-fitting Lorentzian is the dashed line. Lorentzian fits are good for high $|m|/l$ but degrade as $|m|$ decreases. The input intrinsic Q in each case is 10^4, although a value of 9976 is estimated for the $m = -61$ state and a value of 5094 for the $m = 0$ state, which illustrates the that modal coupling can broaden spatially filtered spectral lines considerably.

the structure of the eigenvector matrix for these multiplets. The dependence on intrinsic Q continues to higher intrinsic Q-values. As can be seen in Figure 11, the apparent Q measurement for nearly zonal resonances of ${}_3S_{61}$ is systematically depressed from the intrinsic Q-value and saturates at approximately 15,000, whereas apparent Q measurements for sectoral resonances closely approximate the intrinsic Q. Attempts to measure average apparent degenerate Q must be informed that Q can vary appreciably with m. Wise estimators of intrinsic Q should concentrate on the sectoral ($m \sim l$) resonances and radial resonances ($l = 0$) to minimize this effect. Fortunately, the m-dependence is simple. Figure 12 illustrates that, except for small undulations, a parabola does a good job of fitting the apparent Q profile for the multiplet ${}_3S_{61}$ with $Q_k = 10^4$. For obvious reasons, we refer to the line-broadening effect of convection as the *Q-bowl*.

Figures 10, 11, and 12 display the convective line broadening for just two multiplets. To determine the systematics of this signature of convection, we now consider the apparent quality factors for a suite of low- and intermediate-degree multiplets. In Figures 13 and 14 we display line-broadening trends with n, l, and ω similarly to the way frequency splittings are shown in Figures 8*a*–8*c*. We plot in Figure 13 the variation in apparent Q for the $m = 0$ state as a function of the multiplet index, and in Figures 14*a* and 14*b* we show the dependence of apparent quality factors on the expansion coefficients q_0 and q_2 defined in equation (21).

Figure 13 presents the value of the minimum apparent Q estimate within each multiplet. This will occur for the $m = 0$ state, and we present $Q^0_{k,\mathrm{app}}$ in the normalized form $1 - Q^{(m=0)}_{k,\mathrm{app}}/Q_k$ for the same set of multiplets used in the computation of the frequency splitting coefficients. The minimum value for the normalized form on the plot is 0.55, which corresponds to a minimum apparent Q of 4500, though the input Q is 10^4. A more robust measure of the line-broadening effect of convection is the multiplet expansion coefficients, q^k_0 and q^k_2, of equation (21). The q^k_0 coefficient represents the apparent degenerate frequency, and the q^k_2 coefficient represents the depth of the Q-bowl. These coefficients are displayed in Figures 14*a* and 14*b*, respectively. Since these coefficients are estimated from the $(2l + 1)$ generalized resonance functions of each multiplet, they are more easily measured than the apparent Q for any single generalized resonance function. Kelly & Ritzwoller (1993) discuss methods for their estimation using least-squares techniques.

Figure 15 shows line-width effects as a function of harmonic degree and degenerate frequency. As shown in Figure 15*a*, the minimum apparent quality factors, $Q^0_{k,\mathrm{app}}$, and the apparent degenerate Q's q_0, tend to decrease with increasing l, since there are more states available for coupling. For these two parameters a smaller value indicates a bigger effect. For q_2, the larger the parameter the larger the effect, and q_2 is seen to increase with l in Figure 15*a*. Thus, line-width effects tend to increase with harmonic degree along a dispersion branch for the multiplets we consider here. As Figure 15*b*, shows, line-width effects tend to decrease with frequency, however. This is because we have taken intrinsic Q to be constant, so that intrinsic line widths increase with frequency. As the discussion about Figures 10*a* and 10*b* indicated, convective line broadening decreases as intrinsic line width increases. The magnitude,

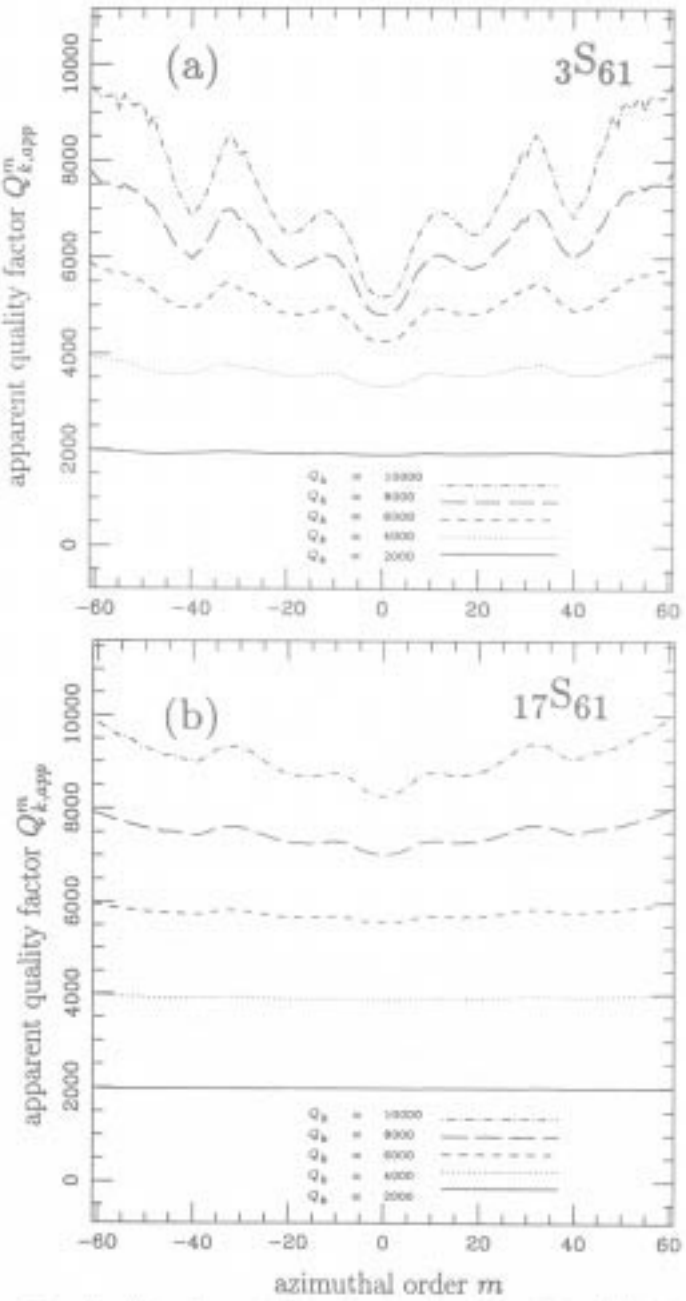

FIG. 10.—Plots of apparent Q as a function of m, $Q^m_{k,app}$, for two different multiplets with values of input intrinsic Q ranging from 2×10^3 to 10^4 in increments of 2×10^3. Results are shown for (*a*) $_3S_{61}$ ($\omega_k = 1.78515$ mHz) and (*b*) $_{17}S_{61}$ ($\omega_k = 4.59904$ mHz). Clearly, the size of the apparent Q effect is a strong function of the intrinsic Q of the mode, and observations of the Q-bowl will be easiest for low-frequency modes where intrinsic Q is highest. The Q-bowl is shallower for $_{17}S_{61}$ than it is for $_3S_{61}$, since intrinsic line widths increase with frequency because we have taken intrinsic Q to be constant.

but not the general character, of all of these effects depends strongly on intrinsic Q.

Figures 12, 14*a*, and 14*b* display the most important results of this paper. The apparent degenerate Q of each multiplet should be depressed relative to the intrinsic Q. In addition, due to the strong dependence of the coupling strength on the frequency splitting profile established by the differential rotation, the nearly parabolic m-dependence of the line widths is a

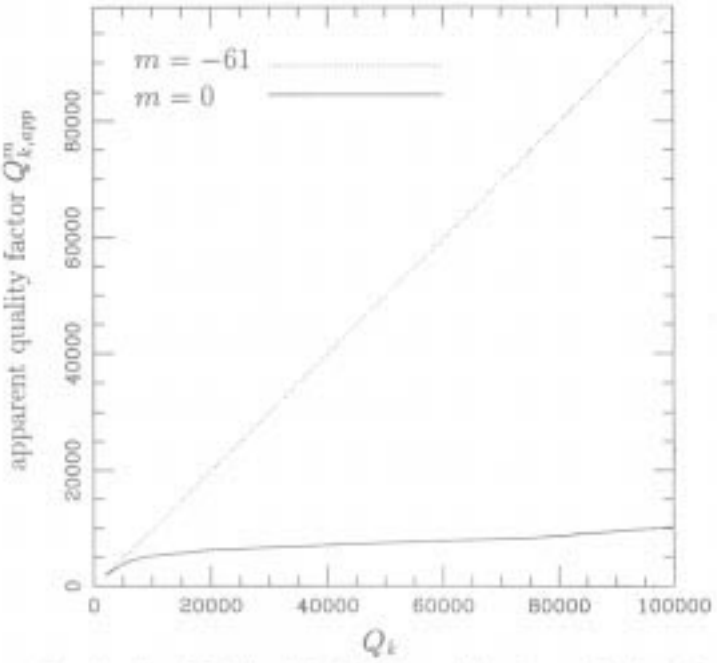

FIG. 11.—Plot of $Q^{m=0}_{app}$ and $Q^{m=-1}_{app}$ for the multiplet $_3S_{61}$ as a function of intrinsic Q. The apparent Q of the $m = 0$ state is greatly reduced by convective line-broadening, saturating at about 15,000. The apparent Q of the $m = -l$ state is only weakly affected by convective line broadening.

robust characteristic and should, therefore, be a reliable signature of global-scale convective flows in helioseismic data. The depth of the Q-bowl is diagnostic of the strength of convection, but is also a function of the degenerate Q of the multiplet. However, since the size of the q_2 coefficient varies slowly with l

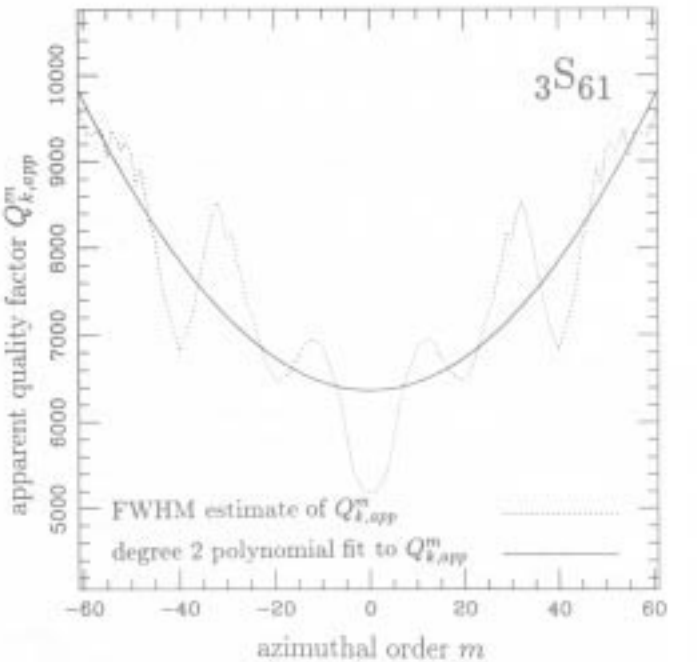

FIG. 12.—Degree $m = 2$ Legendre polynomial fit (*solid line*) to $Q^m_{k,app}$ (*dotted line*) (see eq. [21]) for the multiplet $_3S_{61}$. The input intrinsic Q is 10^4. For this multiplet, $q^k_0 = 7524.3$ (with standard deviation 47.7) and $q^k_2 = 2304.0$ (with standard deviation 105.5). Except for small undulations, the Q variation is well fitted by a parabola in m.

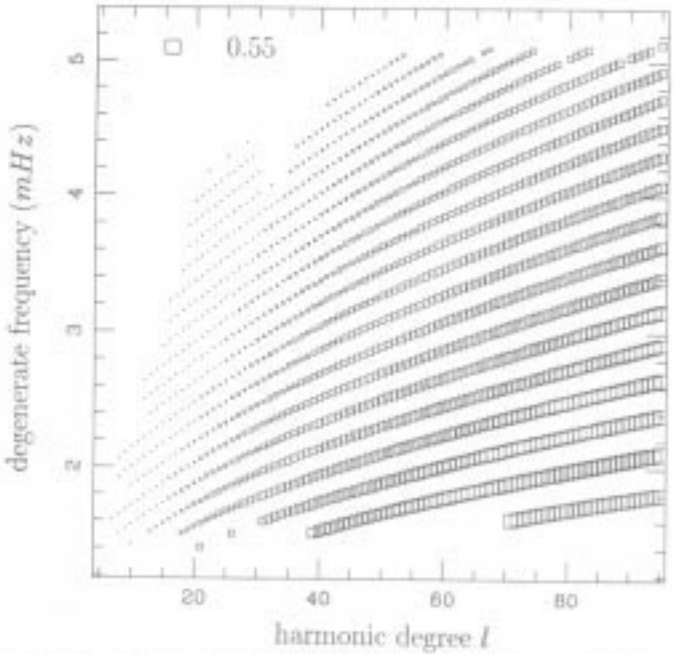

FIG. 13.—Representation similar to Fig. 8 of $Q_{k,app}^{m=0}$ in the normalized form $1 - Q_{k,app}^{m=0}/Q_k$, where $Q_k = 10^4$, for the same suite of multiplets as in Fig. 8. The minimum apparent Q within each multiplet is given by $Q_{k,app}^{m=0}$. For example, for $1 - Q_{k,app}^{m=0}/Q_k = 0.55$, the minimum apparent Q within each multiplet is $Q_{k,app}^{m=0} = 4500$.

and ω_3 it provides little information about the geometry of convection. In § 6 we will discuss how q_0 and q_2 vary with the magnitude of the convective flow velocities.

6. DISCUSSION

Since inversions for differential rotation normally ignore nonaxisymmetric flows, it is important to determine the effect that nonaxisymmetric convection is likely to have on estimates of the differential rotation profile. We have shown that the frequency signal produced by Glatzmaier's model of nonaxisymmetric convection is below the noise level of observational frequency estimates. Thus, the bias introduced by Glatzmaier's convection model is minimal. However, it is important to remember that our frequency splittings are probably lower bounds for two reasons: First, Glatzmaier does not model velocity fields in the top 5% of the Sun (by radius) where the convective velocities are largest. Thus, the frequency perturbations that we have calculated can place only a lower bound on the bias caused by nonaxisymmetric convection. Second, since we have not modeled the effect of poloidal flows on modal coupling, our estimates of the frequency perturbations are conservative.

More important, we wish to consider how the effect of large-scale convection can be observed in helioseismic data. The major observational line-width signatures are (1) a nearly m-parabolic variation of apparent Q within a multiplet, (2) a decrease in apparent degenerate Q, and (3) an increase of importance of the line-width effect with harmonic degree l (everything else being equal). In addition, (4) there should be no convective line broadening for radial ($l = 0$) modes. We will consider each of these in turn.

First, the strongest observational support of the convective line-broadening effect would be the detection of a systematic m-parabolic line-width signature represented by the q_2^k expansion coefficient in equation (21). (This dominantly parabolic behavior of line widths produced by convective line broadening is illustrated in Fig. 12.) Unfortunately, line-width measurements of individual m-states from intermediate- and high-degree multiplets are not yet available. In their absence we must look elsewhere for the effect of convection.

Second, instead of making line-width measurements on individual m-states, observers have commonly linearly recombined the $(2l + 1)$ resonance functions associated with the m-states of a given multiplet. This operation produces a single "stacked"

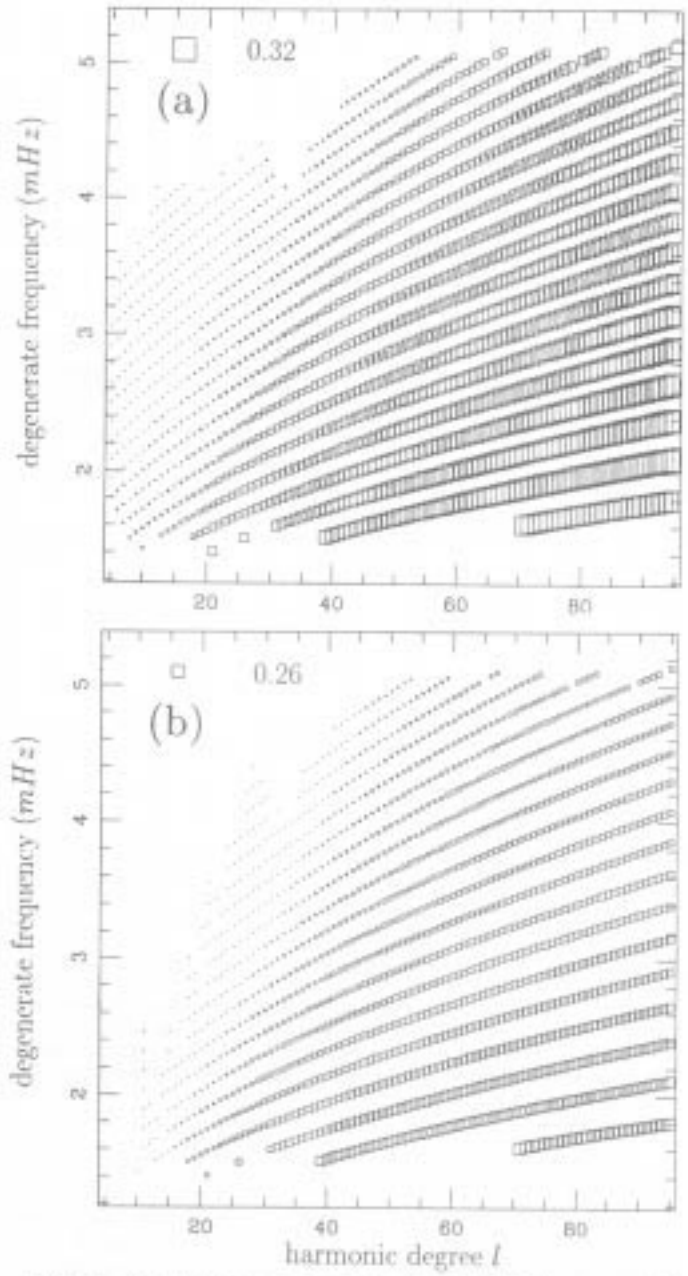

FIG. 14.—Representation, similar to Figs. 8 and 13 for the same set of multiplets, of the coefficients q_j^k (see eq. [21]) in the normalized form $1 - q_j^k/Q_k$, where $Q_k = 10^4$: (a) $j = 0$, from which the apparent degenerate Q can be estimated; (b) $j = 2$, which represents the depth of the Q-bowl. For example, for $1 - q_0^k/Q_k = 0.32$, $q_0^k = 6800$.

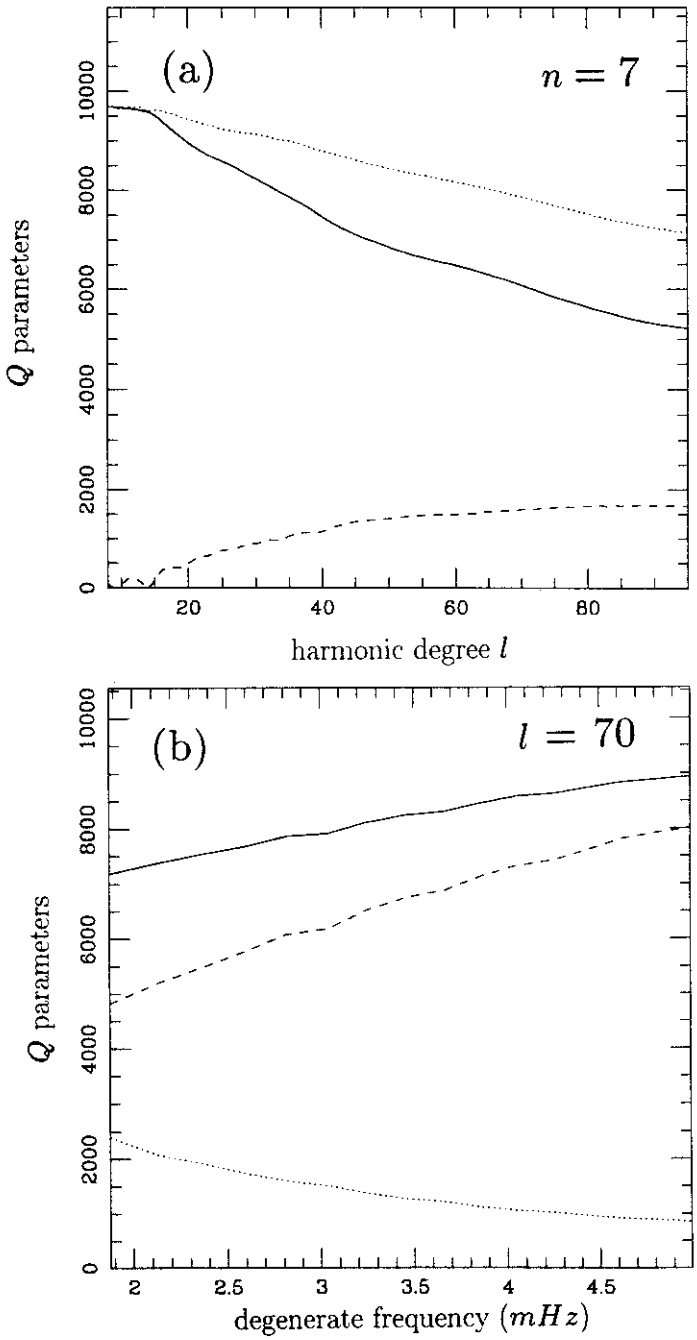

FIG. 15.—Harmonic degree and frequency dependence of $Q_{k,\mathrm{app}}^{(m=0)}$ (*solid line*), (*dotted line*), and q_2^k (*dashed line*). Line-width effects increase with harmonic degree due to the increase in the number of available coupling partners with l. Line-width effects decrease with frequency, since we have taken intrinsic line widths to increase with frequency.

resonance function with an improved signal-to-noise ratio that yields an apparent degenerate Q measurement, but eliminates the m-dependent signal that is the hallmark of large-scale convection. (Studies of such apparent degenerate Q's include Libbrecht 1988, Christensen-Dalsgaard et al. 1989, and Jeffries et al. 1991.) Figure 1 of Christensen-Dalsgaard et al. (1989) displays the observed line widths from Libbrecht (1988) versus theoretical line widths for various models of intrinsic damping processes. Each of the damping models underpredicts the line widths of acoustic modes with frequencies below approximately 2.5 mHz, as do the models of Balmforth (1992a) (see Figs. 4*b* and 5*b* in his paper). Since convective line broadening is most pronounced for modes with low intrinsic damping rates, it is plausible that at least part of the mismatch in theoretical and observed line widths for low-frequency modes may be explained by the convective line-broadening effect. As can be seen from Table 1 of Libbrecht (1988) and Figure 9*a* of Libbrecht & Woodard (1991), the line widths of modes with frequencies greater than about 3.5 mHz are so large that the line-broadening effect of modal coupling is likely to be negligible.

Third, an additional characteristic feature of convective line broadening is its increasing strength with increasing l. This trend is illustrated in Figure 15*a*, and we have explained it in § 5 as follows: The coupling of m-states from the SNRNMAIS model produces the line broadening. Multiplets with large harmonic degrees have more states available for coupling, and the total frequency range spanned by these states increases as l increases. The combined effect produces the l-dependence seen in Figure 15*a*. This relationship between l and line width is qualitatively consistent with the observed l-dependence of helioseismic line widths. Figure 9*b* in Libbrecht & Woodard (1991) shows modal line widths averaged over the frequency interval 2.4 mHz $< \omega <$ 3.0 mHz, as a function of spherical harmonic degree l. The authors suggest that the trend of increasing line width with increasing l is due to the fact that, at constant frequency, modes with higher l have larger surface amplitudes (which would lead to increased damping) than lower l modes. However, this observational trend is also consistent with convective line broadening, which may explain part of the observed trend.

Finally, a very important way of distinguishing convective line broadening effects from intrinsic damping is by observation of the line widths of radial modes, i.e., modes with $l = 0$ and arbitrary radial order n. It is clear from the above discussion and from equation (19) that radial modes are insensitive to the convective line-broadening effect, since there is only one m-state ($m = 0$) for each multiplet ${}_nS_0$. Thus, observed line widths of radial modes should be produced solely by intrinsic damping. A plot of theoretical and observed line widths of radial acoustic modes is shown in Figure 3*a* of Balmforth & Gough (1990). The agreement is quite good, even at frequencies less than 3 mHz. In comparison, the discrepancy in line width for low-frequency modes with nonzero l in Figure 1 in Christensen-Dalsgaard et al. (1989) is considerable. Our results predict that the match between theoretical and observed line widths worsens with increasing l, consistent with the observations described by Balmforth & Gough (1990).

Therefore, to the best of our knowledge, all existing Q estimates are consistent with line broadening caused by large-scale convection. However, to establish unequivocally the existence of giant cells, it is important that m-dependent line-width measurements should soon be estimated. Because of the nature of the m-dependence of the convective line-broadening effect, intrinsic Q measurements should concentrate on nearly sectoral modes, whereas searches for the effect of giant cells should concentrate on the apparent Q difference between nearly zonal modes and nearly sectoral modes. Kelly & Ritzwoller (1993) discuss a method that should be successful in retrieving apparent Q variations of the size predicted by Glatzmaier's model.

The observation of the helioseismic signature of convection would provide the strongest support to date for the existence of

giant cells. If the signal is not observed with methods similar to those of Kelly & Ritzwoller (1993), then it is likely either that giant cells are less vigorous than predicted by current convection theories or that degenerate Q's are less than the values we have used here. To minimize this latter possibility, observers should concentrate first on the lowest possible frequencies, where intrinsic Q-values are highest. The successful observation of the helioseismic effect of convection would mean that statistical constraints could be placed on the strength of convection, though probably little if any geometrical information could be retrieved from line broadening alone. It should be remembered that any large-scale nonaxisymmetric field would produce a similar line-broadening pattern, but it is not yet clear whether any other field is large enough in magnitude to have a measurable effect. Nevertheless, it would prove very interesting to attempt to observe time variations in the line widths and, perhaps, track the strength of convection deep in the solar interior over a solar cycle. It is likely that this goal is overly ambitious using line-width measurements alone.

We have discussed at some length the dependence of the line-broadening effects of convection on l, ω, and intrinsic Q. Another obvious free variable is the size of the input convective model, which up until now we have chosen to be Glatzmaier's model described in § 2.1. Figure 16 displays the effect on the expansion coefficients q_0 and q_2 of ${}_3S_{61}$ of varying the size of the nonaxisymmetric components of Glatzmaier's model, where, again, we have chosen input intrinsic Q to be 10^4. Thus, we fix the nonaxisymmetric geometry of Glatzmaier's velocity model, but vary its size. Consider a new input model $f(r, \theta, \phi) = \beta w(r, \theta, \phi)$, where β merely scales the nonaxisymmetric components of Glatzmaier's model $w(r, \theta, \phi)$, leaving the axisymmetric components unchanged. For the experiments reported above, $\beta = 1$. As Figure 16 shows, the apparent degenerate Q, q_0, decreases nearly linearly with β, from 10^4 for the axisymmetric model ($\beta = 0$) to approximately 4000 for Glatzmaier's model scaled up by a factor of $\beta = 3$. Since q_0 changes rapidly with the size of the input model, it provides a good indicator of model size. The "vertical relief" in the Q-bowl, which is represented by the q_2 parameter, is not such a simple function of β. As the size of the nonaxisymmetric components increases, coupling among m-states significantly away from $m = 0$ increases. The bowl becomes systematically broader at the bottom and is not as well fitted by a simple parabola. Consequently, the q_2 coefficient tends to saturate. The q_2 coefficient cannot effectively discriminate between Glatzmaier's model and, say, the model in which his nonaxisymmetric components are scaled up by a factor of 2. The use of line-width coefficients to constrain the strength of large-scale convection, therefore, will require their simultaneous interpretation and care. Ultimately, q_0 may provide tighter constraints on the magnitude of convective velocities than q_2, though its use requires a knowledge of the intrinsic Q for each multiplet. This will depend on the development of better theoretical models of intrinsic damping or on better measurements of intrinsic Q coming, perhaps, from intensive study of the nearly sectoral resonances and $l = 0$ resonances which are least likely to be broadened by convective modal coupling.

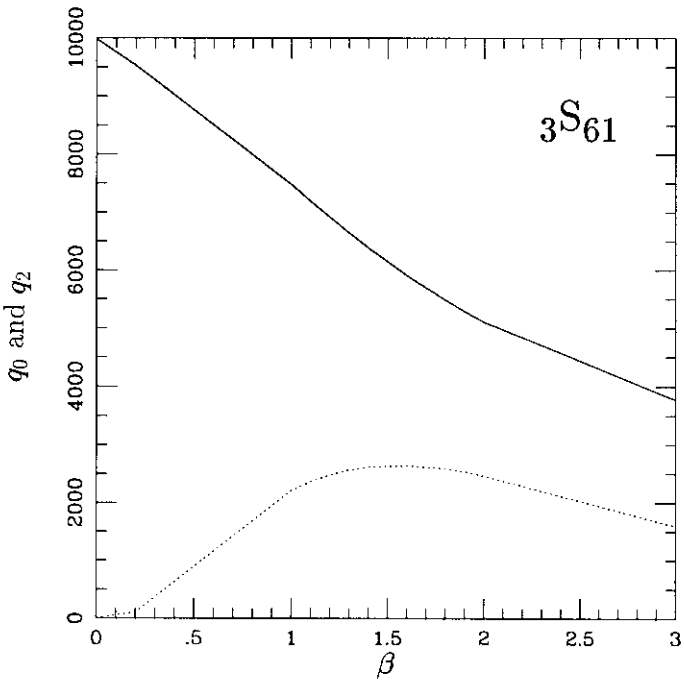

FIG. 16.—Plot of q_0^k (*solid line*) and q_2^k (*dotted line*) for ${}_3S_{61}$ vs. the scaling parameter β defining the size of the convection model. The input convection model is $f(r, \theta, \phi) = \beta w(r, \theta, \phi)$, where w represents the toroidal part of Glatzmaier's model defined in § 2.1.

7. CONCLUSION

This paper presents the numerical application of the theoretical formalism of Lavely & Ritzwoller (1992) to the model of large-scale convection described by Glatzmaier (1984). Its purpose is to discover a measurable signature of convection which can be sought to help establish the existence of solar giant cells and, perhaps, constrain their general features. The formalism of Lavely & Ritzwoller (1992) is based on a number of assumptions, including the assumption that the convective flow field is steady state and anelastic and that the governing equations of motion are linearizable in the mode displacement and convective flow field. Lavely & Ritzwoller (1992) argue that these assumptions are accurate in the region where Glatzmaier's model is defined. A more troubling assumption is that the flow field is steady in time. Although the time dependence of the flow field would affect the details of the results presented here, the general characteristics of the principal results upon which we focus are not affected by it. For example, the selection rules presented by Lavely & Ritzwoller (1992) would still hold for a nonstationary flow field, and line widths would still be broadened, though the degree of broadening would change with time.

The computation of helioseismic frequencies and line widths requires the construction of synthetic helioseismic velocity fields. In this study, synthetic velocity fields are themselves based on three practical assumptions. First, since turbulent convection is the likely source of helioseismic oscillations, we have applied the random phase approximation, which states that the components of the source vector can be considered to be uncorrelated. Second, to simplify the numerical experiments, we have employed degenerate perturbation theory, which couples only degenerate SNRNMAIS modes rather than quasi-degenerate perturbation theory, which allows modes to couple that are only nearly degenerate in the SNRNMAIS model. Finally, and most significantly, we present only ensemble-average results which are the expected value of results from a large number of observing intervals. The focus on ensemble-average results insulates us from explicitly simulating the source of acoustic oscillations. Kelly & Ritzwoller

(1993) discuss methods by which ensemble-average results can be estimated from a single observing run, and in a later contribution will discuss explicit simulations of the acoustic excitation field.

The results presented in this paper may be considered conservative for three reasons. First, we have employed degenerate perturbation theory rather than the more accurate quasi-degenerate perturbation theory, implying that we have effectively ignored aspects of the flow field that should contribute to convective line broadening. Second, Glatzmaier's model runs only to 0.95 $R_\odot$ and, therefore, does not include contributions from the high-velocity flows near the surface. Finally, the FWHM method of measuring Q yields smaller Q variations than the methods that are designed by Kelly & Ritzwoller (1993) to work effectively on real data. However, we have attempted to offset these factors by choosing an input intrinsic Q model that is high, at least for modes above 2 mHz.

The principal conclusion of this paper is that the most significant helioseismic signature of large-scale convection should be a systematic, dominantly m-parabolic line-width effect within each multiplet. This line-broadening effect for certain resonances exceeds 50% of the intrinsic Q for Glatzmaier's model. The magnitude of this effect is a strong function of the intrinsic Q, and we have taken intrinsic Q to be approximately 10^4. The source of this m-parabolic signature is easy to understand. The width of a generalized resonance function depends on the degree of coupling to neighboring SNRNMAIS modes. If the range of frequencies over which coupling is significant is broad compared with the intrinsic line width, then the resulting resonance will be broadened. Frequency splittings are controlled by differential rotation which has a characteristic pattern with m. Different m-values are more closely spaced for low $|m|/l$ than for high $|m|/l$. Therefore, coupling will be strongest among low-$|m|/l$ modes. This is why the low-$|m|/l$ modes are preferentially broadened relative to the high-$|m|/l$ modes. Helioseismic frequencies also are shifted by large-scale convection, but not as significantly relative to measurement error as line widths. Nevertheless, they possess distinctive patterns that could be exploited to estimate their effect on measured frequencies.

To establish the existence of convective giant cells, and perhaps to estimate their statistical characteristics, it should become a priority to measure individual m-state line widths in the future. Current Q measurements have been made by linearly recombining the $2l + 1$ resonances within a multiplet to produce a high signal-to-noise measurement of degenerate Q. Our numerical results predict three effects of large-scale convection on degenerate Q: (1) degenerate Q measurements should be lower than intrinsic Q, (2) the line-width broadening should increase with harmonic degree l, and (3) radial ($l = 0$) modal line widths should be unaffected by large-scale convection. All three of these predictions are consistent with current observations. The magnitude of the nonaxisymmetric components of the model also affects the magnitude and character of the line-width effect. This will be the subject of further study.

We are very grateful to Gary Glatzmaier for providing us with a numerical model of convection, without which this study could not have been completed, and to Juri Toomre for suggesting its use. Adrian van Ballegooijen's help throughout this study has been exceptional. We would like to thank Ronald Gilliland for providing us with a solar model and stellar evolution code and John Woodhouse for modifying his eigenfunction code for application to the Sun. Ken Libbrecht generously provided his splitting coefficients and error estimates which informed our discussion of differential rotation. We thank Tim Brown, Thomas Bogdan, Douglas Gough, and Pawan Kumar for many valuable discussions. We are grateful to John Kelly for his collaboration on this project and for constructing Figure 9. E. M. L. was supported by a postdoctoral fellowship from the Advanced Study Program and the High Altitude Observatory at NCAR. This work was also supported by the National Science Foundation under grants PHY89-04035, ATM-88-05194, ATM-88-05546; by NASA under grant NAGW-1677; and by the National Center for Supercomputing Applications at the University of Illinois, Urbana-Champaign under grant xfo. The National Center for Atmospheric Research is supported by the National Science Foundation.

APPENDIX A

MODAL NOTATION AND TERMINOLOGY

In this appendix we introduce the notation and terminology that we use to define and characterize the acoustic wave field. A spherical, nonrotating, nonmagnetic adiabatic, isotropic, static solar model is referred to as a SNRNMAIS solar model. A mode of such a model is uniquely identified by a single triple of quantum numbers (n, l, m) that denote, respectively, the radial order, the harmonic degree, and the azimuthal order of the mode. A modal frequency of a SNRNMAIS solar model is simply the degenerate frequency of the multiplet ${}_nS_l$ that comprises the $(2l + 1)$ modes with identical n and l values. The degenerate frequency is denoted by ω_k, where k is the multiplet index (n, l). Any symmetry-breaking agent such as rotation, magnetic fields, or convection will lift this $(2l + 1)$ degeneracy and split the frequencies of the modes composing the multiplet. If the symmetry-breaking agent is axisymmetric, as is differential rotation, then to a good approximation the spatial structure of each mode will remain specified by the same triple of quantum numbers. For a general, nonaxisymmetric perturbation, each modal eigenfunction is a linear combination of the eigenfunctions of the SNRNMAIS solar model. The expansion coefficients under degenerate perturbation theory are given by the components of the eigenvectors of the splitting matrix $\mathbf{H}_k$ (defined in Appendix B). It is of dimension $(2l + 1) \times (2l + 1)$, and is composed of the block-diagonal general matrix elements $H^{m'm}_{nn,ll}$ $(-l \le m' \le l, -l \le m \le l)$.

Since the acoustic modes are spheroidal, the vector eigenfunctions $s^m_k(\mathbf{r})$ of the SNRNMAIS solar model can be written in the form

$$s^m_k(\mathbf{r}) = {}_nU_l(r)Y^m_l(\theta, \phi)\hat{\mathbf{r}} + {}_nV_l(r)\nabla_1 Y^m_l(\theta, \phi)\,, \tag{A1}$$

where ${}_nU_l(r)$ and ${}_nV_l(r)$ are the scalar radial eigenfunctions, and the time dependence is given by $\exp(i\omega_k t)$. The coordinates (r, θ, ϕ)

are spherical polar coordinates (where θ is the colatitude) and $\hat{\boldsymbol{r}}$, $\hat{\boldsymbol{\theta}}$, $\hat{\boldsymbol{\phi}}$ denote unit vectors in the coordinate directions. The surface gradient operator is given by

$$\nabla_1 = \hat{\boldsymbol{\theta}} \frac{\partial}{\partial \theta} + \frac{\hat{\boldsymbol{\phi}}}{\sin \theta} \frac{\partial}{\partial \phi} . \tag{A2}$$

The function $Y_l^m(\theta, \phi)$ is a spherical harmonic of degree l and azimuthal order m defined using the convection of Edmonds (1960):

$$\int Y_{l'}^{m'*}(\theta, \phi) Y_l^m(\theta, \phi) \sin \theta \, d\theta \, d\phi = \delta_{m'm} \delta_{l'l} , \tag{A3}$$

where the asterisk denotes the complex conjugate, and the integration is performed over the unit sphere. The vector eigenfunctions satisfy an orthogonality condition given by

$$\int \rho_0(r) \mathbf{s}_{k'}^{m'*}(\boldsymbol{r}) \cdot \mathbf{s}_k^m(\boldsymbol{r}) r^2 \sin \theta \, d\theta \, d\phi \, dr = \int_0^{R_\odot} \rho_0(r) [{}_n U_l^2(r) + l(l+1) {}_n V_l^2(r)] r^2 dr \, \delta_{m'm} \delta_{n'n} \delta_{l'l}$$
$$= N_k \delta_{m'm} \delta_{n'n} \delta_{l'l} , \tag{A4}$$

where $R_\odot$ denotes the radius at the solar surface and $\rho_0(r)$ is the density of the solar model.

Seismic toroidal modes are excluded from the seismic basis set, since these modes are of zero or near-zero frequency and therefore will not significantly interact with acoustic poloidal modes in the frequency range of interest (1.5 mHz $\leq \nu \leq$ 5.0 mHz).

APPENDIX B

SUMMARY OF DEGENERATE PERTURBATION THEORY

Degenerate perturbation theory is an approximation to quasi-degenerate perturbation theory that governs modal coupling and splitting. Under this theory, only those modes that share the same degenerate frequency in the SNRNMAIS solar model are allowed to couple. Using this fact, the principal result of degenerate perturbation theory follows immediately from quasi-degenerate perturbation theory (Lavely & Ritzwoller 1992):

$$\boldsymbol{\Lambda}^{(k)} = \mathbf{A}^{(k)\dagger} \mathbf{H}_k \mathbf{A}^{(k)} , \tag{B1}$$

where $\boldsymbol{\Lambda}^{(k)}$ is a diagonal matrix of eigenvalues $\delta\omega_j$ ($-l \leq j \leq l$), $\mathbf{A}^{(k)}$ is the unitary eigenvector matrix that diagonalizes the splitting matrix $\mathbf{H}_k$, and k denotes the multiplet ${}_n S_l$. The (m', m) component of $\mathbf{H}_k$ is given by

$$H_{nl}^{m'm} = \frac{i}{N_k} \left[\int \rho_0 \, \mathbf{s}_k^{m'*}(\boldsymbol{r}) \cdot \boldsymbol{\Omega} \times \mathbf{s}_k^m d^3 r + \int \rho_0 \, \mathbf{s}_k^{m'*}(\boldsymbol{r}) \cdot \boldsymbol{u}_0 \cdot \nabla \mathbf{s}_k^m d^3 r \right] , \tag{B2}$$

where $-l \leq m' \leq l$, $-l \leq m \leq l$, and N_k is given by equation (A4). In writing equation (B2), we neglected contributions from perturbations to the density, adiabatic bulk modulus, gravitational potential, ellipticity of figure, and centripetal acceleration (the matrix elements for these perturbations are given in Lavely & Ritzwoller 1992). In terms of the modal eigenfunctions and the expansion coefficients of the toroidal velocity field, $H_{nl}^{m'm}$ can be written

$$H_{nl}^{m'm} = \delta_{mm'} m\Omega \int_0^{R_\odot} \rho_0 (2UV + V^2) r^2 dr + (-1)^{m'} (2l+1) \sum_{s=1}^{\infty} \gamma_s \sum_{t=-s}^{s} \begin{pmatrix} l & s & l \\ -m' & t & m \end{pmatrix} \int_0^{R_\odot} \rho_0(r) w_s^t(r) T_s(r) r^2 dr , \tag{B3}$$

where the kernel $T_s(r)$ is given by

$$T_s(r) = -l(l+1) r^{-1} \{2UV - U^2 - V^2 [l(l+1) - \tfrac{1}{2} s(s+1)]\} \begin{pmatrix} l & s & l \\ -1 & 0 & 1 \end{pmatrix} , \tag{B4}$$

and γ_s is given by

$$\gamma_s = \left(\frac{2s+1}{4\pi} \right)^{1/2} \tag{B5}$$

The Wigner 3-j symbols in equations (B3) and B4) are defined according to the phase convention of Edmonds (1960).

The frequency splitting in the corotating frame due to differential rotation and the Coriolis force are given by the diagonal elements of the splitting matrix (see Ritzwoller & Lavely 1991; Lavely & Ritzwoller 1992):

$$\omega_k^m = \omega_k + \delta\omega_m = \omega_k + \frac{1}{N_k} \left[m\Omega \int_0^{R_\odot} \rho_0 \, C(r) r^2 dr + \sum_{s=1,3,5,\ldots} \gamma_{sl}^m \int_0^{R_\odot} w_s^0(r) {}_n K_{sl}(r) r^2 dr \right] , \tag{B6}$$

where

$${}_n K_{sl}(r) = \rho_0 r^{-1} [2UV + \tfrac{1}{2} s(s+1) V^2 - U^2 - l(l+1) V^2] \tag{B7}$$

and the coefficient γ_{sl}^m is defined in equation (33) of Ritzwoller & Lavely (1991). The frequencies ω_k^m in the inertial frame are obtained by subtracting $m\Omega$ from the right-hand side of equation (B6).

APPENDIX C

THEORETICAL WAVE FIELDS AND POWER SPECTRA

C1. THE ACOUSTIC WAVE FIELD IN THE INERTIAL FRAME

The helioseismic displacement field given by equation (1) is calculated in the corotating frame. Since helioseismic Doppler images are ordinarily measured from the Earth's surface, it is necessary to transform the displacement field to a frame other than the Sun's. In this paper we identify the observer's frame with an inertial frame. As discussed in § 2 of Lavely & Ritzwoller (1992), the transformation to an inertial frame is accomplished by the variable transformation $\phi \rightarrow \phi - \Omega t$, where Ω is the average angular rotation rate at the solar surface. Noting that the dependence of $s_k^m(\mathbf{r})$ on the azimuthal angle ϕ is given by $\exp(im\phi)$, and using index notation for clarity, equation (1) can be written

$$u_k^\sigma(\mathbf{r}, t) = \sum_{j=-l}^{l} \sum_{m=-l}^{l} A_{mj}^{(k)} s_k^m(\mathbf{r}) \sum_{i=-l}^{l} A_{ji}^{(k)\dagger} a_i^{\sigma k}(t) * \lambda_{mj}^{(k)}(t) , \tag{C1}$$

where $\lambda_{mj}^{(k)}(t)$ is given by

$$\lambda_{mj}^{(k)}(t) = \exp(i\omega_{jk}^m t) \exp(-\alpha_k t) , \tag{C2}$$

ω_{jk}^m is given by

$$\omega_{jk}^m = \omega_k - m\Omega + \Lambda_{jj}^{(k)} , \tag{C3}$$

and $\Lambda_{jj}^{(k)}$ $(-l \leq j \leq l)$ are the components of the diagonal matrix $\mathbf{\Lambda}^{(k)}$. By the convolution theorem, we obtain in the frequency domain

$$u_k^\sigma(\mathbf{r}, \omega) = \sum_{j=-l}^{l} \sum_{m=-l}^{l} A_{mj}^{(k)} s_k^m(\mathbf{r}) \sum_{i=-l}^{l} A_{ji}^{(k)\dagger} a_i^{\sigma k}(\omega) \lambda_{mj}^{(k)}(\omega) . \tag{C4}$$

The Lorentzian function $\lambda_{mj}^{(k)}(\omega)$ is given by

$$\lambda_{mj}^{(k)}(\omega) = \frac{1}{2}\left[\frac{1}{\alpha_k + i(\omega - \omega_{jk}^m)}\right] , \tag{C5}$$

where we have neglected the contribution from the pole $\alpha_k + i(\omega + \omega_{jk}^m)$.

C2. SYNTHETIC POWER SPECTRA

In practice, helioseismic time series are obtained by the application of a spherical harmonic spatial filter to a sequence of Doppler images. Similarly, a synthetic time series of a convecting model is calculated by application of the spatial filter to the time derivative of the theoretical wave field in equation (2). In this section we calculate this time series and its power spectrum. Since modes in the convecting model are coupled, it is not possible to extract from Doppler images the time series and power spectrum that correspond to a single mode of oscillation, as can be done with a spherically symmetric or differentially rotating model. Instead, the time series and power spectrum are computed for the motion associated with a single spherical harmonic. The resulting power spectrum will contain resonant lines from each mode in the convecting model that depends on the spherical harmonic.

The complex time series $F_k^{m'}(t)$ associated with the target spherical harmonic $Y_l^{m'}(\theta, \phi)$ of the kth multiplet is given by

$$F_k^{m'}(t) = \int Y_l^{m'*}(\theta, \phi) f(\theta, \phi) g(t) \hat{\mathbf{e}}_{\text{los}} \cdot \sum_\sigma \partial_t \mathbf{u}_k^\sigma(\mathbf{r}, t) \sin\theta \, d\theta \, d\phi , \tag{C6}$$

where $\hat{\mathbf{e}}_{\text{los}}$ is the line-of-sight vector, $g(t)$ is a time-domain filter that accounts for gaps and tapers, and $f(\theta, \phi)$ is a weighting function applied to down-weight noise contamination near the solar limb [e.g., Tomczyk 1988 used $f(\theta, \phi) = \sin^2\theta \cos^2\phi$]. In practice, only one hemisphere of the Sun can be imaged, and so the integration is performed only over the visible solar disk $(0 \leq \theta \leq \pi, -\pi/2 \leq \phi \leq \pi/2)$. The acoustic wave field in equation (C6) is evaluated at the radius where the observed velocity field is imaged. The time series $F_k^{m'}(t)$ contains contributions from displacement patterns with quantum numbers nearly similar to the target quantum numbers m' and l. This aliasing is due to the line-of-sight vector, the weighting function, the imaging of one hemisphere only, and the finite resolution of the observed Doppler image. Each of these effects can be modeled as in equation (C6), but for simplicity we neglect them here by (1) assuming that the sampling of the wave field over θ and ϕ is continuous, (2) performing the integral in equation (C6) over the entire sphere, and (3) defining $f(\theta, \phi) = g(t) = 1$, and $\hat{\mathbf{e}}_{\text{los}} = \hat{\mathbf{r}}$.

After adopting the simplifications described above, the complex spectrum is obtained by substituting equation (C1) into equation (C6) taking the Fourier transform, and performing an integration by parts:

$$F_k^{m'}(\omega) = i\omega \, {}_nU_l \sum_{j=-l}^{l} A_{m'j}^{(k)} \sum_{i=-l}^{l} A_{ji}^{(k)\dagger} \sum_\sigma a_i^{\sigma k}(\omega) \lambda_{m'j}^{(k)}(\omega) . \tag{C7}$$

The power spectrum is given by $|F_k^{m'}(\omega)|^2$:

$$|F_k^{m'}(\omega)|^2 = {}_nU_l^2 \omega^2 \sum_{j=-l}^{l} \sum_{j'=-l}^{l} A_{m'j}^{(k)} A_{m'j'}^{(k)*} \sum_{i=-l}^{l} \sum_{i'=-l}^{l} A_{ji}^{(k)\dagger} A_{j'i'}^{(k)*\dagger} \sum_\sigma \sum_{\sigma'} a_i^{\sigma k}(\omega) a_{i'}^{\sigma' k*}(\omega) \lambda_{m'j}^{(k)}(\omega) \lambda_{m'j'}^{(k)*}(\omega) . \tag{C8}$$

C3. WAVE-FIELD STATISTICS: THE RANDOM PHASE APPROXIMATION

The existence of many acoustic sources and the turbulent nature of near-surface convection suggest that a statistical approach to the calculation of power spectra is in order. We use the random phase approximation to simplify equation (15). In our application, the random phase approximation asserts that

$$\sum_{\sigma'}\sum_{i'} a_i^{\sigma k}(\omega)a_{i'}^{\sigma' k*}(\omega) = \sum_{\sigma'=\sigma}\sum_{i'=i} a_i^{\sigma k}(\omega)a_{i'}^{\sigma' k*}(\omega) + \sum_{\sigma'\neq\sigma}\sum_{i'\neq i} a_i^{\sigma k}(\omega)a_{i'}^{\sigma' k*}(\omega)$$
$$= \sum_{\sigma} |a_i^{\sigma k}(\omega)|^2 \delta_{\sigma\sigma'}\delta_{ii'} . \tag{C9}$$

The second equality follows from the first, since phase randomization ensures that the components that contribute to the second summation destructively interfere.

It is known from the observation of helioseismic oscillations that all $(2l+1)$ m-states of a given multiplet are excited to approximately equal energies. In terms of the source coefficients, we are led to conclude that

$$\sum_{\sigma} |a_i^{\sigma k}(\omega)|^2 = |b_k(\omega)|^2 \qquad \text{for all } i . \tag{C10}$$

The dependence of this sum on i, together with the random phase approximation, leads to considerable simplification of our expression for the power spectrum. Using equations (C9) and (C10), we can rewrite equation (C8) in the form

$$|F_k^{m'}(\omega)|^2 = {}_nU_l^2\omega^2 \sum_{j=-l}^{l}\sum_{j'=-l}^{l} A_{m'j}^{(k)}A_{m'j'}^{(k)*}\left\{\sum_{i=-l}^{l}\sum_{i'=-l}^{l} A_{ji}^{(k)\dagger}A_{j'i'}^{(k)*\dagger}\delta_{ii'}\right\}|b_k(\omega)|^2\lambda_{m'j}^{(k)}(\omega)\lambda_{m'j'}^{(k)*}(\omega) . \tag{C11}$$

The expression in curly brackets can be simplified as follows:

$$\sum_{i=-l}^{l}\sum_{i'=-l}^{l} A_{ji}^{(k)\dagger}A_{j'i'}^{(k)*\dagger}\delta_{ii'} = \sum_{i=-l}^{l} A_{ji}^{(k)\dagger}A_{j'i}^{(k)*\dagger}$$
$$= \delta_{jj'} , \tag{C12}$$

where we have used the unitarity property of the eigenvector matrix $\mathbf{A}^{(k)}$, i.e.,

$$\mathbf{A}^{(k)\dagger}\mathbf{A}^{(k)} = \mathbf{I} . \tag{C13}$$

Equations (C11) and (C12) together yield

$$|F_k^{m'}(\omega)|^2 = {}_nU_l^2\omega^2 \sum_{j=-l}^{l}\sum_{j'=-l}^{l} A_{m'j}^{(k)}A_{m'j'}^{(k)*}|b_k(\omega)|^2\delta_{jj'}\lambda_{m'j}^{(k)}(\omega)\lambda_{m'j'}^{(k)*}(\omega)$$
$$= {}_nU_l^2\omega^2|b_k(\omega)|^2 \sum_{j=-l}^{l} |A_{m'j}^{(k)}|^2|\lambda_{m'j}^{(k)}(\omega)|^2$$
$$= \frac{{}_nU_l^2\omega^2|b_k(\omega)|^2}{4} \sum_{j=-l}^{l} \frac{|A_{m'j}^{(k)}|^2}{\alpha_k^2 + (\omega - \omega_{jk}^{m'})^2} . \tag{C14}$$

APPENDIX D

SPECTRAL ANALYSIS OF SYNTHETIC DATA

In this appendix we describe the techniques that we have used to estimate apparent frequencies and apparent quality factors from generalized resonance functions of the convecting model in the ensemble average. More generally useful methods that are designed for use on real data are discussed in Kelly & Ritzwoller (1993). In § 4 we discussed the problems inherent in estimating these quantities from non-Lorentzian functions. We refer to the *apparent* frequency and the *apparent* quality factor, since these quantities are not unambiguously defined to a generalized resonance function. We have chosen to use the first-moment and FWHM (full width half-maximum) methods to estimate frequencies and line widths, respectively, since these methods are commonly used by observers.

We now consider the first-moment method of estimating frequencies. The power spectrum $|\mathscr{L}_0(\omega)|^2$ of a Lorentzian satisfies the identity

$$\int_{-\infty}^{\infty} (\omega - \omega_0)|\mathscr{L}_0(\omega)|^2 d\omega = 0 , \tag{D1}$$

where ω_0 is the frequency centroid, and in the time-domain the Lorentzian function $\mathscr{L}_0(t)$ is given by $A_0 \exp(-\alpha_0 t)\cos(\omega_0 t)$, and in general A_0 is complex. Thus, ω_0 is the ratio of the first and zeroth moments of the power spectrum. Modeling the generalized resonance function as a Lorentzian, the estimator $\omega_{k,\text{app}}^{m'}$ of the apparent frequency is given by

$$\int_{-\infty}^{\infty} (\omega - \omega_{k,\text{app}}^{m'}) < |F_k^{m'}(\omega)|^2 > d\omega = 0 . \tag{D2}$$

Substituting equation (19) in equation (D2), and evaluating the integral, we obtain

$$\omega_{k,\mathrm{app}}^{m'} = \sum_{j=-l}^{l} |A_{m'j}^{(k)}|^2 \omega_{jk}^{m'} \Big/ \sum_{j=-l}^{l} |A_{m'j}^{(k)}|^2 \tag{D3}$$

Thus, $\omega_{k,\mathrm{app}}^{m'}$ is the weighted sum of the frequencies associated with the eigenvectors of the splitting matrix $\mathbf{H}_k$, and the weights are given by the squared moduli of the components of the m'th row of the eigenvector matrix $\mathbf{A}^{(k)}$.

We use the FWHM method to estimate line widths. With this method models can include the effect of time-domain tapers. Such a correction was not applied in our numerical analysis, since $g(t)$ in equation (C6) was set to unity. Since observed time series are of finite length, we consider the effect of the boxcar taper on line-width estimates. Thus, we set $g(t) = [H(0) - H(T)]$, where T is the time-series length, and $H(t)$ is the Heaviside step function. The power spectrum of $g(t)\mathscr{L}_0(t)$ is given by

$$|\mathscr{L}_0(\omega)|^2 = \frac{|A_0|^2}{\alpha_0^2 + (\omega - \omega_0)^2} \{1 + e^{-2\alpha_0 T} - 2e^{-\alpha_0 T} \cos [(\omega - \omega_0)T]\} , \tag{D4}$$

and is peaked at $\omega = \omega_0$ for arbitrary (α_0, T). For $T = \infty$, the half-maximum values of the power spectrum are at the frequencies $\omega_0 \pm \alpha_0$. Thus, α_0 is often referred to as the half-width of the Lorentzian. The line width Γ_0 is related to the quality factor Q_0 by the expression

$$\Gamma_0 = 2\alpha_0 = \frac{\omega_0}{Q_0} . \tag{D5}$$

For a time series of length T, the ratio of the power spectrum at $\omega_0 \pm \alpha_0$ to its peak value at ω_0 is given by

$$\frac{|\mathscr{L}_0(\omega_0 \pm \alpha_0)|^2}{|\mathscr{L}_0(\omega_0)|^2} = \frac{1}{2}\left[\frac{1 + e^{-2\alpha_0 T} - 2e^{-\alpha_0 T} \cos (\alpha_0 T)}{1 + e^{-2\alpha_0 T} - 2e^{-\alpha_0 T}}\right], \tag{D6}$$

where the factor in brackets models the effect of finite T. Equation (D6) can be solved for α_0 iteratively. In the first iteration, we set $T = \infty$, and determine from the synthetic resonance function the two frequencies that correspond to the half-maximum values. This yields an initial estimate of α_0. The correction factor in square brackets in equation (D6) can then be computed, two new values of frequencies are obtained (which yield a new value of α_0), and so forth. In our synthetic experiments, we find that this procedure typically converges in just a few iterations for a wide range of input (α_0, T) values, provided that the frequency bins are small enough. Clearly, expressions similar to equation (D6) can be derived for other tapers.

REFERENCES

Backus, G. E., & Mulcahy, M. 1976a, Geophys. JRAS, 46, 341
———. 1976b, Geophys. JRAS, 47, 301
Balmforth, N. 1992a, MNRAS, 255, 603
———. 1992b, MNRAS, 255, 632
———. 1992c, MNRAS, 255, 639
Balmforth, N., & Gough, D. O. 1990, ApJ, 362, 256
Bogdan, T. 1989, ApJ, 339, 1132
Brown, T. M. 1984, Science, 226, 687
———. 1990, ApJ, 371, 396
Brown, T. M., Christensen-Dalsgaard, J., Dziembowski, W. A., Goode, P., Gough, D. O., & Morrow, C. A. 1989, ApJ, 343, 526
Cattaneo, F., Brummell, N. H., Toomre, J., Malagoli, A., & Hurlburt, N. E. 1991, ApJ, 370, 282
Christensen-Dalsgaard, J., Gough, D. O., & Libbrecht, K. G. 1989, ApJ, 341, L103
Christensen-Dalsgaard, J., Schou, J., & Thompson, M. J. 1990, MNRAS, 242, 353
Dahlen, F. A. 1979, Geophys. JRAS, 58, 1
Edmonds, A. R. 1960, Angular Momentum in Quantum Mechanics (Princeton: Princeton Univ. Press)
Gilman, P. A., & Glatzmaier, G. A. 1981, ApJS, 45, 335
Gilman, P. A., & Miller, J. 1986, ApJS, 61, 585
Glatzmaier, G. A. 1984, J. Comput. Phys., 55, 461
Glatzmaier, G. A., & Gilman, P. A. 1981, ApJS, 45, 351
———. 1982, ApJ, 256, 316
Goldreich, P., & Kumar, P. 1988, ApJ, 326, 462
Goode, P. R., Gough, D., & Kosovichev, A. 1992, ApJ, 387, 707
Hart, J. E., Glatzmaier, G. A., & Toomre, J. 1986b, J. Fluid Mech., 173, 519
Hart, J. E., et al. 1986a, Science, 234, 61
Hill, F. 1988, ApJ, 333, 996
———. 1989, ApJ, 343, L69
Hill, F., Toomre, J., & November, L. J. 1983, Sol. Phys., 82, 41
Jeffries, S. M., Duvall, T. L., Harvey, J. W., Osaki, Y., & Pomerantz, M. W. 1991, ApJ, 377, 330
Kelly, J., & Ritzwoller, M. H. 1993, ApJ, in press
Kumar, P., & Goldreich, P. 1989, ApJ, 342, 558
Lavely, E. M., & Ritzwoller, M. H. 1992, Phil. Trans. R. Soc. Lond., A, 339, 431
Libbrecht, K. G. 1988, ApJ, 334, 510
Libbrecht, K. G., & Woodard, M. 1991, Science, 253, 152
Libbrecht, K. G., Woodard, M., & Kaufman, J. 1990, ApJS, 74, 1129
Masters, G., & Gilbert, F. 1983, Phil. Trans. R. Soc. Lond., A, 308, 479
Ritzwoller, M. H., & Lavely, E. M. 1991, ApJ, 369, 557
Schulten, K., & Gordon, R. G. 1975, J. Math. Phys., 16, 1971
Smith, B. T., Dongarra, J. J., Gabrow, B. S., Ikebe, Y., Klema, V. C., & Moler, C. B. 1976, Matrix Eigensystem Routines—EISPACK Guide (Lecture Notes in Computer Science, Vol. 6; Berlin: Springer-Verlag)
Spruit, H., Nordlund, A., & Title, A. 1990, ARA&A, Vol. 28
Stein, R., & Nordlund, A. 1989, ApJ, 342, L95
Thompson, M. J. 1990, Sol. Phys., 125, 1
Tomczyk, S. 1988, Ph.D. thesis, Univ. California, Los Angeles
Woodhouse, J. H. 1988, in Seismological Algorithms, ed. D. J. Doornbos (San Diego: Academic), 321
Zare, R. N. 1988, Angular Momentum: Understanding Spatial Aspects in Chemistry and Physics (New York: Wiley)